The experimental data raise the question of whether the suppression of baseline CBF and evoked CBF by NS-398 is due to COX-2 inhibition or whether it is a side-effect of DMSO and/or metabolites, which could provoke non-specific changes in other biochemical pathways involved in the regulation of neurovascular coupling. From the results of the comparative analysis between control and COX-2 inhibition, we revealed that the baseline CBF decreased within 1-h of infusion of NS-398, reaching a plateau thereafter (dotted line in Fig. 4). Significant decreases in normalized evoked CBF were detected after NS-398 infusion within 2.5–3.5 h in spite of the non-suppression of neuronal activity (Figs. 6 and 7B), when the normalized evoked CBF after COX-2 inhibition was comparable with that of the control measurement. Moreover, we have reported in our previous study that the normalized evoked CBF is not affected by a change in baseline CBF (Matsuura et al., 2000). These observations suggest that NS-398 affects the decreases in baseline CBF and evoked CBF due to COX-2 inhibition, and that the decreases in baseline and evoked CBF were regulated by separate mechanisms because of the difference in the duration of NS-398 efficacy. It is well known that the change in MABP should not affect CBF due to the auto-regulation system in brain circulation (Paulson et al., 1990). There is a possibility that COX-2 affects the regulation of local CBF during neuronal activation in rats although there are side-effects of solvent and/or metabolites.

References

Ances, B.M., 2004. Coupling of changes in cerebral blood flow with neuronal activity: what must initially dip must come back up. J. Cereb. Blood Flow. Metab. 24, 1–6.

Bakalova, R., Matsuura, T., Kanno, I., 2002. The cyclooxygenase inhibitors Indomethacin and Rofecoxib reduce regional cerebral blood flow evoked by somatosensory stimulation in rats. Exp. Biol. Med. (Maywood) 227, 465–473.

Chaigneau, E., Oheim, M., Audinat, E., Charpac, S., 2003. Two- photon imaging of capillary blood flow in olfactory bulb glomeruli. Proc. Natl. Acad. Sci. U.S.A. 100, 13081–13086.

Chalon, S., Vancassel, S., Zimmer, L., Guilloteau, D., Durand, G., 2001. Polyunsaturated fatty acids and cerebral function: focus on monoaminergic neurotransmission. Lipids 36, 937–944.

Detre, J.A., Ances, B.M., Takahashi, K., Greenberg, J.H., 1998. Signal averaged laser-Doppler measurements of activation-flow coupling in the rat forepaw somatosensory cortex. Brain Res. 796, 91–98.

Del Bigio, M., James, H.E., Camp, H.E., Werner, R., Marshall, L.F., Tung, H., 1982. Acute dimetyl sulfoxide therapy in brain edema. Part 3. Effect of a 3-hour infusion. Neurosurgery 10, 86–89.

Dudeck, O., Jordan, O., Hoffmann, K.T., Okuducu, A.F., Tesmer, K., Kreuzer-Nagy, T., Rufenacht, D.A., Doelker, E., Felix, R., 2006. Organic solvents as vehicles for precipitating liquid embolics: a comparative angiotoxic study with superselective injections of swine rete mirabile. Am. J. Neuroradiol. 27, 1900–1906.

Girouard, H., Iadecola, C., 2006. Neurovascular coupling in the normal brain and in hypertension, stroke, and Alzheimer disease. J. Appl. Physiol. 100, 328–335.

Hameroff, S.R., Otto, C.W., Kanel, J., Weinstein, P.R., Blitt, C.D., 1981. Acute cardiovascular effects of dimetylsulfoxide. Crit. Care Med. 9, 855–857.

Iadecola, C., 2004. Neurovascular regulation in the normal brain and in Alzheimer's disease. Nat. Rev. Neurosci. 5, 347–360.

Lauritzen, M., 2005. Reading vascular changes in brain imaging: is dendritic calcium the key? Nat. Rev. Neurosci. 6, 77–85.

Kagan, V., Bakalova, R., Koynova, G., Tyurin, V., Serbinova, E., Petkov, V.V., Petkov, V.D., Staneva, D., Packer, L., 1992. Antioxidant protection in the brain against oxidative stress. In: Packer, L., Prilipko, L., Christen, Y. (Eds.), Free Radicals in the Brain: Aging, Neurological and Mental Disorders. Springer Verlag, Berlin, pp. 49–61.

Magistretti, P.J., Pellerin, L., Rothman, D.L., Shulman, R.G., 1999. Energy demand. Science 22, 496–497.

Matsuura, T., Fujita, H., Seki, C., Kashikura, K., Kanno, I., 1999. Evoked CBF change by somatosensory activation measured by laser-Doppler flowmetry: independent evaluation of RBC velocity and RBC concentration. Jpn. J. Physiol. 49, 289–296.

Matsuura, T., Fujita, H., Kashikura, K., Kanno, I., 2000. Evoked local cerebral blood flow induced by somatosensory stimulation is proportional to the baseline flow. Neurosci. Res. 38, 341–348.

Matsuura, T., Kanno, I., 2001. Quantitative and temporal relationship between local cerebral blood flow and neuroral activation induced by somatosensory stimulation in rats. Neurosci. Res. 40, 281–290.

Ngai, J.A., Meno, J.R., Winn, H.R., 1995. Stimulation of pial arteriolar diameter and laser-Doppler flow during somatosensory stimulation. J. Cereb. Blood Flow Metab. 15, 124–127.

Niwa, K., Araki, E., Moeham, S.G., Ross, M.E., Iadecola, C., 2000. Cyclooxygenase-2 contributes to functional hyperemia in whisker-barrel cortex. J. Neurosci. 15, 763–770.

Paulson, O.B., Strandgaard, S., Edvinsson, L., 1990. Cerebral auto-regulation. Cerebrovasc. Brain Metab. Rev. 2, 161–192.

Phillis, J.W., Horrocks, L.A., Farooqui, A.A., 2006. Cyclooxygenases, lipoxygenases, and epoxygenases in CNS: their role and involvement in neurological disorders. Brain Res. Rev. 52, 201–243.

Solfrizzi, V., D'Introno, A., Colacicco, A.M., Capurso, C., Del Parigi, A., Capurso, S., Gadaleta, A., Capurso, A., Panza, F., 2005. Dietary fatty acids intake: possible role in cognitive decline and dementia. Exp. Gerontol. 40, 257–270.

Takano, T., Tian, G.-F., Peng, W., Lou, N., Libionka, W., Han, X., Nedergaard, M., 2006. Astrocyte-mediated control of cerebral blood flow. Nat. Neurosci. 9, 260–267.

Wang, X., Lou, N., Xu, Q., Tian, G.-F., Peng, W.G., Han, X., Kang, J., Takano, T., Nedergaard, M., 2006. Atrocytic Ca^{2+} signaling evoked by sensory stimulation in vivo. Nat. Neurosci. 9, 816–823.

Yehuda, S., Rabinovitz, S., Carasso, R.L., Mostofsky, D.I., 2002. The role of polyunsaturated fatty acids in restoring the aging neuronal membrane. Neurobiol. Aging 23, 843–853.

Research Article

NMR IN BIOMEDICINE

Received: 3 December 2007, Revised: 23 February 2009, Accepted: 23 February 2009, Published online in Wiley InterScience: 6 May 2009

(www.interscience.wiley.com) DOI:10.1002/nbm.1391

A multi-compartmental SE-BOLD interpretation for stimulus-related signal changes in diffusion-weighted functional MRI

Jeff Kershaw[a], Moyoko Tomiyasu[a], Kenichi Kashikura[b], Yoshiyuki Hirano[a], Hiroi Nonaka[a], Masaya Hirano[c], Hiroo Ikehira[a], Iwao Kanno[a] and Takayuki Obata[a]*

A new interpretation is proposed for stimulus-induced signal changes in diffusion-weighted functional MRI. T_2-weighted spin-echo echo-planar images were acquired at different diffusion-weightings while visual stimulation was presented to human volunteers. The amplitudes of the positive stimulus-correlated response and post-stimulus undershoot (PSU) in the functional time-courses were found to follow different trends as a function of *b*-value. Data were analysed using a three-compartment signal model, with one compartment being purely vascular and the other two dominated by fast- and slow-diffusing molecules in the brain tissue. The diffusion coefficients of the tissue were assumed to be constant throughout the experiments. It is shown that the stimulus-induced signal changes can be decomposed into independent contributions originating from each of the three compartments. After decomposition, the fast-diffusion phase displays a substantial PSU, while the slow-diffusion phase demonstrates a highly reproducible and stimulus-correlated time-course with minimal undershoot. The decomposed responses are interpreted in terms of the spin-echo blood oxygenation level dependent (SE-BOLD) effect, and it is proposed that the signal produced by fast- and slow-diffusing molecules reflect a sensitivity to susceptibility changes in arteriole/venule- and capillary-sized vessels, respectively. This interpretation suggests that diffusion-weighted SE-BOLD imaging may provide subtle information about the haemodynamic and neuronal responses. Copyright © 2009 John Wiley & Sons, Ltd.

Keywords: ADC; biexponential signal decay; diffusion-weighting decomposition; functional MRI; spin-echo BOLD

INTRODUCTION

There has been considerable interest recently in performing diffusion-weighted functional MRI (DW-fMRI) studies. One reason for this is that, with the application of diffusion-weighting (as characterised by the *b*-value (1)), the motion of blood through the irregularly arranged vessels of a single voxel is known to suppress intravascular (IV) signal more strongly than the extravascular (EV) contribution (2,3). Furthermore, it has been argued that for *b*-values in the range 0–250 s/mm^2, the signal from larger arteries and veins is more quickly attenuated than that from smaller vessels such as arterioles, capillaries and venules (4,5). It has therefore been suggested that activation maps based on changes to the apparent diffusion coefficient (ADC) will be more specific to the temporal and spatial characteristics of the neural activity than those based on blood oxygenation level dependent (BOLD) contrast. However, this hypothesis has not been rigorously verified.

At heavier *b*-values (300–1600 s/mm^2), it has been suggested that stimulus-correlated signal changes likely reflect changes in the cerebral blood volume (CBV), which are reportedly more specific to smaller vessels nearest to the neural activation (6). The authors of that study argued that at high *b*-values regions of negative activation, where the signal is decreased by an applied stimulus, predominately correspond to CBV changes, whereas areas of positive activation are predominately related to BOLD changes. It was hypothesised that, as *b* increases the BOLD changes gradually decrease in magnitude while the CBV changes are attenuated to a much smaller extent. Whether this interpretation is adequately supported by experimental data is yet to be established.

In another work it was proposed that, at high *b*-value, changes in the ADC might reflect microstructural changes in neurons or

* *Correspondence to: T. Obata, Department of Biophysics, Molecular Imaging Centre, National Institute of Radiological Sciences, 4-9-1 Anagawa, Inage-ku, Chiba 263-8555, Japan.*
E-mail: t_obata@nirs.go.jp

a *J. Kershaw, M. Tomiyasu, Y. Hirano, H. Nonaka, H. Ikehira, I. Kanno, T. Obata Department of Biophysics, Molecular Imaging Centre, National Institute of Radiological Sciences, 4-9-1 Anagawa, Inage-ku, Chiba 263-8555, Japan*

b *K. Kashikura School of Radiological Technology, Gunma Prefectural College of Health Sciences, 323-1 Kamioki-cho, Maebashi 371-0052, Japan*

c *M. Hirano Imaging Application Technology Centre, GE Yokogawa Medical Systems Ltd, 4-7-127 Asahigaoka, Hino-shi, Tokyo 191-8503, Japan*

Contract/grant sponsor: Ministry of Education, Culture, Sports, Science and Technology (MEXT), Japanese Government.

Abbreviations used: *ADC, apparent diffusion coefficient; BOLD, blood oxygenation level dependence; CBV, cerebral blood volume; DW-fMRI, diffusion-weighted fMRI; EPI, echo-planar imaging; EV, extravascular; FDP, fast-diffusion phase; FIV, fast-IV; fMRI, functional MRI; GE, gradient echo; IV, intravascular; PSCR, positive stimulus-correlated response; PSU, post-stimulus undershoot; ROI, region of interest; SDP, slow-diffusion phase; SE, spin echo; SIV, slow-IV.*

glia during neuronal activity (7). The ability to observe these effects would provide much more precise information about the spatial and temporal characteristics of neural events than observation of the secondary haemodynamic response. Experiments demonstrated that a small but significant and reproducible transient decrease in the ADC is detectable during visual cortex activation. More recently, the ADC change was reinterpreted in terms of a two-phase functional diffusion model, where the rate of diffusion in each phase is independent of time (8). Within this model water molecules are said to undergo a slow exchange between a slow-diffusion phase (SDP) and a fast-diffusion phase (FDP), and the fMRI signal change is understood as an expansion (contraction) of the SDP (FDP) during the application of a stimulus. Hence, it was hypothesised that measuring changes in the SDP expansion coefficient might provide a method for directly observing neuronal activity with fMRI.

Another recent study examined changes to the DW-fMRI signal in the visual cortex of cats at 9.4 T (9). The high in-plane spatial resolution (≈0.3 mm) possible at 9.4 T allowed the authors to separate the middle cortical region from the cortex surface where large draining veins exist. From the data acquired at a range of *b*-values and TEs, it was asserted that signal contributions from the veins need only be considered for short TEs ($\lesssim$20 ms) because the T_2 of venous blood is quite short (≈6 ms) at 9.4 T, whereas the T_2s of tissue and arterial blood are similar so that the remainder of the signal is relatively insensitive to TE. The authors concluded that at longer TEs, when the venous contribution is negligible, and for low *b*-values, the ADC changes in the middle cortical layer most likely originate from a functional increase in arterial blood volume. Moreover, since the arterial contribution is also negligible for *b*-values above 200 s/mm^2 and there was no ADC change detected in the midcortical region, it was argued that the contribution of tissue to ADC change is minimal. In short, the authors conclude that the ADC change originates from the haemodynamic response rather than from changes within the tissue. One shortcoming of this interpretation may be that it is based upon monoexponential signal decay in tissue with respect to *b*, an assumption that is inconsistent with many previous studies of brain diffusion (10–18).

The aim of the present paper is to propose an alternative method for interpreting the stimulus-induced changes in DW-fMRI. Diffusion-weighting was applied during the acquisition of T_2-weighted spin-echo (SE) echo-planar images while visual-stimulation was presented to human volunteers. Rather than analysing in terms of changes to a single ADC, experimental data are interpreted with a signal model having three compartments, two of which are dominated by brain tissue. Each tissue compartment is assumed to have a unique time-independent diffusion constant, and the fMRI signal during brain activation is decomposed into contributions from each compartment. This technique may provide more precise information about the haemodynamic and neural responses.

THEORY

As already noted in the Introduction section, it is widely accepted that the motion of blood in the vessels enhances the attenuation of IV signal when diffusion-weighting is applied (19). It has been suggested that this behaviour may be characterised by a single-exponential decay and a pseudo-diffusion coefficient of order 10^{-2}–10^{-1} mm^2/s, which would indicate that the IV contribution becomes negligible for $b \approx 200$ s/mm^2 (2). However, experiments using perfluorocarbon blood substitutes find that the IV signal decay is biexponential, with the signal from the slower fraction (possibly corresponding to smaller veins where the blood velocity is slowest) persisting for *b*-values of 600 s/mm^2 and perhaps higher (20,21). Therefore, to allow for the possibility that the IV signal is not completely attenuated by a *b*-value of 200 s/mm^2, it is assumed that the IV signal consists of fast-IV (FIV) and slow-IV (SIV) contributions, with the FIV signal at time *t* modelled as

$$S_{\mathrm{FIV}}(t,b) = \begin{cases} S_{\mathrm{FIV}}(t), & b = 0 \\ 0, & b \geq 200 \end{cases} \qquad (1)$$

Note that this equation does not specify the functional form of $S_{\mathrm{FIV}}(t, b)$ for $0 < b < 200$ s/mm^2 because no data will be acquired in that range. Also, consideration of the SIV contribution will be taken up in the Discussion section.

Many studies of diffusion in brain tissue have suggested that, in the resting state, for *b*-values greater than 1000 s/mm^2, a biexponential diffusion model may be used to describe the attenuation of an NMR signal (10–18). Accordingly, it is proposed here that for diffusion-weighting greater than 200 s/mm^2 the total fMRI signal may be decomposed into contributions from two compartments with distinct diffusion coefficients ($D_{\mathrm{f}} \gg D_{\mathrm{s}}$)

$$S(t,b) = S_{\mathrm{FDP}}(t)\mathrm{e}^{-bD_{\mathrm{f}}} + S_{\mathrm{SDP}}(t)\mathrm{e}^{-bD_{\mathrm{s}}}, \quad b \geq 200 \qquad (2)$$

In writing down this equation it has been assumed that exchange between the FDP and SDP is slow in comparison to the measurement time-scale (typically 60–120 ms in diffusion-weighted SE echo-planar imaging (EPI)), specifying that the rate constants of the exponentials are equal to the diffusion coefficients of the two compartments (22). However, present knowledge of water diffusion in brain tissue is insufficient to conclusively rule out the existence of exchange. When significant exchange exists, the rate constants are much more complicated functions of the diffusion coefficients, rate of exchange, gradient strength and sequence timing parameters (22–24). That is, the true diffusion coefficients of the water pools will differ from the observed rate constants. Nevertheless, as the values of D_{f} and D_{s} to be used in the analysis are empirically obtained, the results of this paper will be independent of any exchange that may be taking place.

A further assumption used in eqn (2) is that the diffusion coefficients are constant during neuronal activation so that the time-dependence of the signal is entirely contained in $S_{\mathrm{FDP}}(t)$ and $S_{\mathrm{SDP}}(t)$. This assumption is based on the premise that the activated state is a perturbation of normal brain function. It is expected that changes to the viscosity and other intrinsic physical characteristics affecting the motion of *in vivo* water will be negligible during neural activity. Likewise, it is presumed that deformation of tissue microstructure during activation is very small so that changes to the diffusion coefficients via possible restriction effects will also be insignificant.

METHODS

A visual stimulation study was conducted on eight healthy volunteers (seven males and one female, age 20–31 years). All participants gave their informed written consent and the study was approved by the Institutional Ethics Committee.

NMR Biomed. 2009; **22**: 770–778

DW-fMRI was performed on a whole-body 3 T MRI system (Excite HD, GE Medical Systems, Milwaukee, WI) equipped with an eight-channel phased-array head coil and a 40 mT/m actively shielded whole-body magnetic field gradient. An SE-EPI sequence, sensitised to diffusion by the application of additional gradient pulses along the readout axis on either side of the 180° refocusing pulse, was used to obtain interleaved diffusion-weighted images (1). Different *b*-values were obtained by varying the gradient amplitude while keeping all other parameters constant. The sequence alternated between two *b*-values during acquisition to minimise the effects of motion. The *b*-value pattern was either $b = 1400, 0, 1400, 0, \ldots$ s/mm^2 or $b = 1400, 200, 1400, 200, \ldots$ s/mm^2, with a value of 1400 s/mm^2 used in both examinations to improve the signal-to-noise ratio of images acquired with the larger *b*-value. The echo-time was 71.2 ms, the minimum value allowing a *b*-value of 1400 s/mm^2. A repetition time of 2 s was used for a total of 250 repetitions. Other imaging parameters included a field-of-view of 240 mm × 240 mm, a slice thickness of 5 mm (gap = 2 mm), matrix size 64 × 64, and EPI acquisition time 23.4 ms. A short series of gradient-echo T_2^*-weighted MR images (three cycles of 30 s activation and 30 s rest) was obtained and a rapid analysis of the activated areas was performed to determine the most appropriate slices for DW-fMRI. Two axial slices were chosen. The activation task for DW-fMRI consisted of four cycles of 40 s with an alternating black-and-white flickering checkerboard (8 Hz) followed by 80 s of rest. Visual stimulation was delivered via a PC synchronised with the fMRI acquisition using the Presentation software package (Neurobehavioral Systems, Inc., Albany, CA).

Data postprocessing was performed with in-house software written for Matlab (Mathworks Inc., Natick, MA). After smoothing (3 × 3 spatial + 3-point temporal box filters), five central time points during stimulation (~20–40 s after onset) and ten post-stimulation points (~80–120 s after onset) were selected and a Student *t* test analysis was used to identify the activated pixels. By simply comparing the signal levels during periods where the signal change might be reasonably expected to be at its maximum (i.e. the middle of the stimulus period and after the return-to-baseline), this simple activation analysis has the advantage that presumptions about the shape of the positive stimulus-correlated response (PSCR) are minimised. Also, whether the averaged time-courses contain a post-stimulus undershoot (PSU) is not predetermined by the pixel selection criterion. Pixels in the primary visual area with *t*-values of more than 4 ($p < 0.0001$, uncorrected for multiple comparisons) for both the $b = 200$ and 1400 s/mm^2 images were designated as activated. The activated set was further filtered by discarding pixels that, by eye, clearly overlapped a sulcus or other region containing a significant CSF fraction. Mean responses were obtained for each subject by averaging the intensities of the selected pixels across cycles and pixels. The mean responses were then averaged across subjects to arrive at the final DW-fMRI time-courses. For the purpose of evaluating the dependence of the PSCR and PSU on *b*-value, the mean value of the baseline interval 108–120 s after stimulus onset was subtracted from the mean values of the intervals 28–40 s (PSCR) and 56–68 s (PSU) after stimulus onset.

The decomposition of the DW-fMRI time-courses into FIV, FDP and SDP contributions was performed by assuming that at each time point t_n

$$S(t_n, b) = S_{\mathrm{FIV}}(t_n, b) + S_{\mathrm{FDP}}(t_n)\mathrm{e}^{-bD_{\mathrm{f}}} + S_{\mathrm{SDP}}(t_n)\mathrm{e}^{-bD_{\mathrm{s}}} \qquad (3)$$

describes the signal as a function of *b*, with the assumptions of the three-compartment model stipulating that $S_{\mathrm{FIV}}(t_n, b) = 0$ for $b \geq 200$ s/mm^2. Explicit dependence of the signal on TE is not included in the equation because all experiments in this work are performed at the same echo-time. To minimise errors due to the 2 s offset between images acquired with $b = 1400$ s/mm^2 and those acquired with $b = 0$ or 200 s/mm^2, linear interpolation of the time-courses was performed. That is, at times t_n where $S(t_n, b)$ was not explicitly acquired, $S(t_n, b)$ was approximated by $[S(t_{n-1}, b) + S(t_{n+1}, b)]/2$. As there were only three data points (one corresponding to each *b*-value) from which to estimate the three parameters of the model, the calculation is actually the exact solution of a system of three equations rather than a fitting procedure. Values for the parameters D_{f} and D_{s} were taken from the literature rather than estimated from independent experimental data because the NMR system was limited to *b*-values below 2000 s/mm^2 at the time when the experiments were performed. Attempts to fit a biexponential function to resting-state data did not agree well with previously published diffusion coefficients. In previous work, it has been noted that the deviation from single-exponential decay is subtle within the range 0–2000 s/mm^2, and it is only with much higher *b*-values (>4000 s/mm^2) that a reliable fit to a biexponential function is achieved (23,25). A survey of the literature (16,23–27) found that for humans D_{f} and D_{s} varied between $1.01–1.74 \times 10^{-3}$ and $0.11–0.37 \times 10^{-3}$ mm^2/s. The measurements from Reference (16), $D_{\mathrm{f}} = 1.21 \times 10^{-3}$ mm^2/s and $D_{\mathrm{s}} = 0.16 \times 10^{-3}$ mm^2/s, were close to the median values of these ranges and therefore used as estimates for the diffusion coefficients in the decomposition procedure.

RESULTS

Across the eight subjects, a total of 308 pixels in the visual cortex passed the criteria for activation. The mean fractional responses are shown in Fig. 1a–c. The error bars were calculated as the standard deviation between subjects. For the purposes of comparison, the same three mean responses are plotted together in Fig. 1d. The black horizontal bar denotes the period during which the stimulus was applied.

Figure 2 presents the trends of the PSCR and PSU as a function of *b*. Note that the PSU is relatively unaffected by a *b*-value of 200 s/mm^2, but is substantially reduced when $b = 1400$ s/mm^2 is applied. On the other hand, the PSCR is reduced by $b = 200$ s/mm^2, probably because of the significantly reduced FIV contribution, but increases again for $b = 1400$ s/mm^2. The opposing trends of the PSCR and the PSU suggest that they originate from disparate sources.

In Fig. 3a–c the stimulus-induced signal changes have been decomposed into FIV, FDP and SDP contributions normalised by the observed response for $b = 0$. To demonstrate the fraction that each compartment contributes to the total signal, each response has been plotted with the mean baseline (as a fraction of the $b = 0$ baseline) for that compartment added. The mean baseline for the FIV contribution (0.3 ± 1.6%) is only a small fraction of the total signal, consistent with the *a priori* assumption that it originates from blood. Also, the baseline fractions for the FDP (71.1 ± 2.3%) and SDP (28.7 ± 1.5%) are similar to those found in previous studies of biexponential diffusion-weighted signal decay in brain tissue. The error bars on the functional responses were calculated as the standard deviation between subjects after

NMR IN BIOMEDICINE

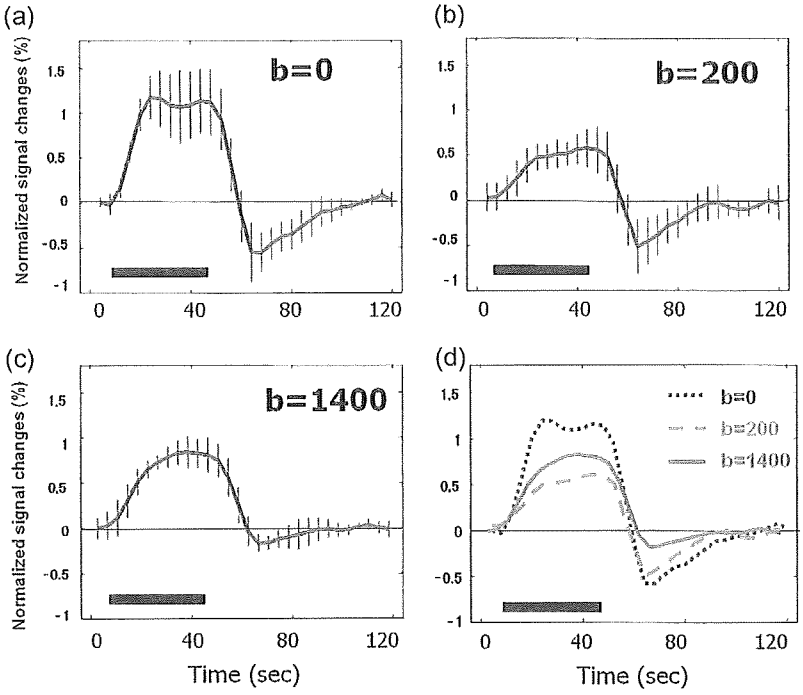

Figure 1. Normalised mean fMRI time courses acquired for b-values of (a) 0 s/mm^2, (b) 200 s/mm^2 and (c) 1400 s/mm^2. The error bars indicate the standard deviation across the eight subjects. (d) Comparison of the mean time-courses presented in (a)–(c). This figure is available in colour online at www.interscience.wiley.com/journal/nbm

removing the baseline values and normalisation. Note that the SDP is more consistent across subjects than the FIV and FDP contributions. All three contributions are further displayed in comparison to the $b = 0$ response in Fig. 3d. An interesting feature is that the SDP time-course shows a positive deflection highly correlated with the stimulation while also having negligible PSU, implying that it closely reflects the neural response without contamination by confounding factors such as the undershoot.

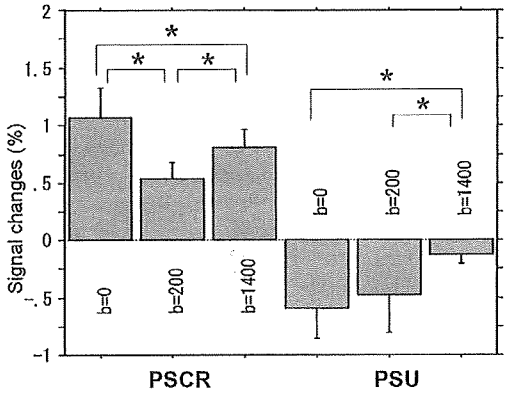

Figure 2. Trends of the positive stimulus-correlated response (PSCR) and post-stimulus undershoot (PSU) with respect to b. The positive response increases for high diffusion-weighting whereas the undershoot is significantly diminished. The stars (*) denote significant differences calculated by a standard analysis of variance (ANOVA) test with Bonferroni–Dunn correction for multiple comparisons ($p < 0.017 \simeq 0.05/3$, where 3 is the number of comparisons).

To determine whether the decomposition results were sensitive to the choice of diffusion coefficients, other values selected from the range of D_f and D_s measurements found in the literature were inserted into the decomposition procedure. Within these ranges, it was found that the decomposed time-courses were not substantially altered. Most importantly, it was verified that the SDP time-course is not an artefact that arises from a fortunate choice of D_f and D_s.

DISCUSSION

Comments on the analysis

As already noted in the Methods section, the decomposition into FIV, FDP and SDP contributions is the exact solution of a system of three equations rather than the result of a fitting procedure. Calculating a number of parameter estimates from the same number of data points is equivalent to the assumption that there is no additive noise and the model parameters explain all variations present in the data. In that case, there is the potential danger that the parameter estimates are meaningless because of the influence of noise originating from sources other than the true signal of interest. In this study, it has been assumed that smoothing the raw-time courses in time and averaging over stimulus trials and activated pixels sufficiently reduced the influence of both spurious fluctuations and low frequency drifts on the decomposition results. Hence, it was not thought that the features of the FIV, FDP and SDP responses were significantly distorted by the limitations of the estimation procedure.

It should be noted that the time-courses displayed in Fig. 1 were calculated from pixels that all showed significant activation and therefore the basic assumption was that those pixels

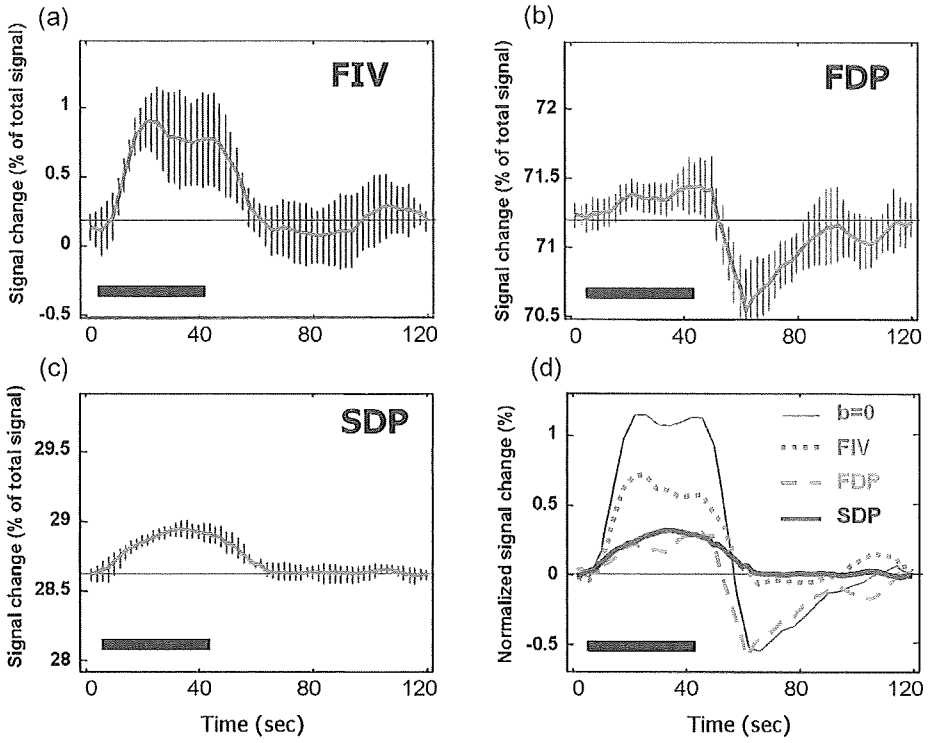

Figure 3. Decomposition of the DW-fMRI time-courses into (a) FIV, (b) FDP and (c) SDP contributions. Each response is normalised by the mean $b = 0$ response in Fig. 1a. Note however that the responses have been plotted with the mean baseline added so that the relative contribution of each component to the total signal is evident from the vertical scale. The horizontal lines are drawn at the baseline level of each component. Baseline values are 0.3 ± 1.6, 71.1 ± 2.3 and $28.7 \pm 1.5\%$ for the FIV, FDP and SDP components, respectively. Error bars illustrate the variation of the decomposed responses over the eight subjects. (d) The baselines of the FIV, FDP and SDP responses have been subtracted so that they may be plotted in comparison to the $b = 0$ response from Fig. 1a. This figure is available in colour online at www.interscience.wiley.com/journal/nbm

primarily contained grey matter. Care was also taken to avoid pixels that clearly overlapped regions containing CSF, although it is possible that some partial-voluming with CSF occurred. As the diffusion constant for CSF has been estimated to be $\sim 2.5 \times 10^{-3}$ mm^2/s (28), a possible CSF contribution would probably be mapped to S_{FIV} or S_{FDP}. Moreover, as the vessels running through CSF space have relatively large radii ($\gtrsim 100\,\mu$m), it can be predicted from literature simulations (29) that the corresponding SE BOLD signal change would be $<0.2\%$ so that weighting on the net signal would be minor. Therefore, it is not expected that CSF will contribute significantly to the functional signal changes.

On a similar note, even though activation is expected to be specific to grey matter, the large pixel-size ($3.75 \times 3.75 \times 5$ mm^3) of these experiments means that most of the pixels will contain both grey and white matter. It is known that white matter has a much higher degree of anisotropy than grey matter, and therefore the results could be sensitive to the imaging plane and direction in which the diffusion-weighting gradients are applied. In fact, it has been noted in earlier work that white matter estimates of D_f and D_s may differ from those in grey matter (23,26,27). However, the difference is not large as the diffusion coefficients for both types of tissue usually lie within the ranges for D_f and D_s quoted at the end of the Methods section. Furthermore, Inglis *et al.* have investigated signal decay in the resting state with a biexponential tensor formalism, finding that anisotropy of the tissue is not the cause of non-exponential behaviour (17). It is therefore not thought that tissue anisotropy affects the results of the decomposition process.

Remarks on previous DW-fMRI studies

The data presented in this paper indicate that the PSCR is reduced for $b = 200$ s/mm^2 but increases again for $b = 1400$ s/mm^2, whereas the PSU is relatively unaffected for $b = 200$ s/mm^2 but is substantially reduced when $b = 1400$ s/mm^2 is applied. In previous DW-fMRI studies with $b > 500$ s/mm^2, maximum attention was focused on the dependence of the PSCR on b-value. Harshbarger and Song (6) (using gradient-echo spiral EPI with human subjects at 4 T) claimed a decrease in BOLD for the b-value range 300–600 s/mm^2, but uncertainty suggests that the decrease is not significant. Le Bihan *et al.* (8) (dual SE, human, 3 T) noted a monotonic increase in the raw signal change as b was increased from 600 to 2400 s/mm^2. Likewise, Miller *et al.* (30) (dual SE, human, 3 T) observed a monotonic increase in signal change (from ~1% to between 2 and 3%) with increasing b-value over the range 0–2400 s/mm^2, although a dip in the PSCR between 0 and 600 s/mm^2 cannot be ruled out as the measurements were made in steps of 600 s/mm^2. Jin *et al.* (9) (single and dual SE EPI, cat, 9.4 T) presented amplitude changes for both middle cortex and surface regions of interest (ROIs). For the middle cortex ROI the signal change decreased from 0 to 200 s/mm^2, but remained almost unchanged when increased to 800 s/mm^2. For the surface ROI, the trend from 0 to 200 s/mm^2 is similar, but the signal change increased when $b = 800$ s/mm^2. Yacoub *et al.* (SE EPI, cat, 9.4 T) also presented results for midcortical and surface ROIs (31). For the midcortical ROI, the signal change decreased from $b = 0$ to 1200 s/mm^2 but increased again at $b = 2400$ s/mm^2, however there was no clear tendency for the surface ROI. It should also be

NMR IN BIOMEDICINE

noted that while none of the above studies quantified the dependence of the PSU on b-value, a PSU appears to remain in the $b = 2400$ s/mm^2 data of Miller *et al.* (30) and perhaps also that of Yacoub *et al.* (31). Although the reasons for the different experimental results are not known, some of the disagreement might depend on the experimental setup through factors such as the type of animal, imaging sequence, acquisition parameters, field strength or stimulus paradigm.

The interpretation of DW-fMRI adopted for this paper is that the signal is the weighted sum of contributions from three independent compartments. Within this description, as the b-value increases the relative contribution to the total signal from a compartment with a large diffusion coefficient is decreased in comparison to those from compartments with smaller rates of diffusion. Eventually, at high b-values the contributions from faster compartments will be negligible and the functional signal change will be dominated by slow compartments. In previous DW-fMRI studies, the time-dependent ADC estimated using a single-exponential tissue-decay model has often been calculated with pairs of diffusion-weighted images (see e.g. References (7,9)). When a non-exponential-decay signal is analysed with a single-exponential model, a discrepancy between the ADCs calculated from two different b-value pairs occurs naturally. Since non-exponential signal attenuation is a well-established fact, this suggests that functional ADC changes cannot be said to generally reflect CBV-weighting, as was proposed in earlier work (6,9).

The data presented in the present paper are consistent with previous DW-fMRI results when analysed in terms of changes to the ADC. Darquie *et al.* calculated ADCs by pairing images acquired at b-values of 200 and ~1450 s/mm^2 (7). During stimulation, there was a small but significant decrease in the ADC followed by a slow return to the prestimulus baseline. When a similar analysis was applied to the data in this paper (Fig. 4a), it was realised that the delayed recovery of the ADC after stimulation ceases is due to the PSU. In another work, Jin *et al.* acquired images at three different b-values and subsequently grouped them into a low b-value pair (2 and 200 s/mm^2) and a large b-value pair (200 and 800 s/mm^2) for the analysis (9). To compare the present data with those results, it must first be noted that the large pixel size in this study ($3.75 \times 3.75 \times 5$ mm^3) does not allow the resolution of separate surface and midcortical grey matter ROIs. Nor is it possible to reliably separate the grey and white matters. Nevertheless, a crude comparison between the two sets of results is possible if the high TE (60 ms) results from Jin *et al.*'s surface and midcortical ROIs are combined. For the low b-value pair, it is expected that combining the surface and midcortical results would give an overall increase in ADC. Doing the same for the high b-value pair would probably reveal a small decrease in ADC during stimulation. This is consistent with the ADCs calculated from the data in the present paper (Fig. 4b).

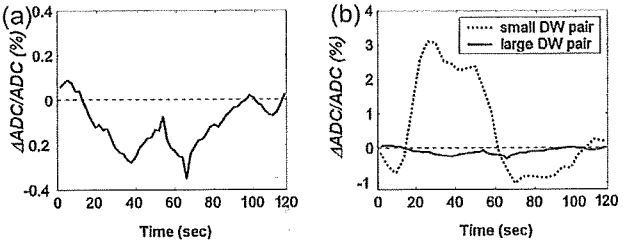

Figure 4. Analysis of the data from Fig. 1 in terms of ADC changes for comparison with the results of Darquie *et al.* (7) and Jin *et al.* (9). (a) Deviation of the ADC calculated from the $b = 200$ and 1400 s/mm^2 data sets. There is a small drop in ADC during the stimulus period followed by a slow return-to-baseline after cessation. (b) Percentage change in ADC for a low b-value pair ($b = 0$ and 200 s/mm^2) and high b-value pair ($b = 200$ and 800 s/mm^2). The $b = 800$ s/mm^2 time-course was estimated using the FIV, FDP and SDP time-courses of Fig. 3 and eqns (2) and (3). Similar to the results of Jin *et al.* there is a substantial positive change for the low b-value pair, whereas there is only a very small negative change for the high b-value pair.

Interpretation of the FDP and SDP signal changes

To date, the functional signal change in SE fMRI was thought to be dominated by the BOLD effect, which under the assumption of slow-exchange is often considered as the sum of IV and EV contributions; that is, $S(t, b) = S_{EV}(t, b) + S_{IV}(t, b)$. Both the IV and EV BOLD signal changes are generated by the haemodynamic response to stimulation. Current theories of the EV SE-BOLD effect are based on the diffusion of water molecules through the blood-vessel-induced field gradients that extend into the surrounding tissue (29,32). Regardless of whether there is an applied stimulus or not, the diffusion of water molecules through the non-uniform field near the vessels irreversibly broadens the phase distribution so that a fraction of the signal is lost at the echo time. When a stimulus is applied, the local cerebral blood flow, cerebral metabolic rate of oxygen consumption and CBV are altered and the accompanying change in susceptibility of the blood causes a small change in the field gradient around the vessels. Subsequently, there is a small change in the local phase distribution that, depending on the deoxyhaemoglobin concentration in the local vasculature, is observed as an increase or decrease in the signal by a few per cent.

The close connection between tissue diffusion and EV SE-BOLD signal indicates that both the SDP and FDP time-courses must contain SE-BOLD-related contributions. Although it has long been recognised that the magnitude of the BOLD signal change may vary as a function of the diffusion coefficient and vessel size (33), the authors are unaware of any work in the BOLD literature that considers the existence of two independently diffusing water pools in brain tissue. Nevertheless, by assuming slow-exchange it is possible to use the results of existing simulations to speculate on the interpretation of the FDP and SDP responses as EV SE-BOLD time-courses (29,34,35). In Reference (29) a scaling law, $\beta = D\mathrm{TE}/R^2$, was derived that allows a set of results calculated for a specific diffusion constant (D) and vessel radius (R) to be applied to a situation with the same β but different D and R. Noting that the largest SE-BOLD signal changes occur when β lies between 2 and 4 (29), it is possible to estimate the range of vessel sizes that are most sensitive to the fast- and slow-diffusion phases. Inserting TE = 71.2 ms, it is estimated that vessels with radius in the range 1.6–2.3 μm initiate the largest signal changes for the slow-diffusing molecules, whereas vessels with radii from 4.8 to 6.8 μm do the same for FDP molecules. Examining the distribution of vessel diameters published by Cassot *et al.* (36), it was found that vessels of radii 1.6–2.3 μm correspond to the smallest capillaries in human cortex, while those with radii 4.8–6.8 μm are probably too large to be capillaries and most likely correspond to arterioles or venules. This simple calculation therefore suggests that the SDP time-course is weighted by changes in capillary-sized vessels, whereas the FDP reflects changes in larger vessels.

It is easy to see that this simple interpretation would be attractive for functional imaging research because it separates the different dynamics of small and large vessels. However, other factors, such as a substantial rate of exchange, might complicate the situation. Another factor to consider is the SIV contribution. According to published data, the rate that the SIV signal is attenuated is similar to that of the FDP, making it difficult to distinguish between these two contributions with diffusion-weighted NMR. Alternatively, it is assumed here that the SIV contribution is already accounted for as a small fraction of the predominantly EV FDP signal. In the resting state, the indistinguishability of the IV and EV contributions to the FDP is not a major concern because the diffusion coefficient of the FDP is empirically determined, and therefore it already includes the effects of the SIV contribution. On the other hand, it may be important in functional experiments because the blood signal can contribute significantly to the functional signal change. Finally, it should also be noted that even though a similar decomposition into compartmental contributions would be possible for gradient echo (GE)-BOLD imaging, the simple interpretation outlined above does not apply because (unlike the SE case) EV GE-BOLD signal changes do not peak as a function of vessel size, meaning that both the SDP and FDP responses would be weighted by larger vessel ($\geq 6\,\mu$m) contributions.

Given the model's inability to distinguish between a shift in volume fraction and changes to the relaxation properties of each component, a non-BOLD contribution to the SDP time-course cannot yet be excluded. The greater consistency of the SDP response across subjects suggests that it is less sensitive to small variations in local anatomy than the FDP response. This presents the possibility that a stimulus-correlated process of tissue origin also contributes to the SDP time-course. A possible candidate is the signal change attributed to cell expansion in Reference (8). In that work, the authors chose an imaging sequence designed to minimise the effects of local susceptibility inhomogeneities, whereby it was hoped that BOLD contribution to the functional signal change would be removed so that only cell-expansion effects would remain. Hence, a comparison with the present results is difficult, but nevertheless there are a number of similarities and differences worth noting. First of all and as remarked earlier, Le Bihan *et al.* interpreted the observed signal change during neural activity in terms of the transfer of water between two phases with different rates of diffusion. The model of eqns (1)–(3) similarly uses two water diffusion coefficients to describe the signal attenuation with respect to *b*. However, the present model also allows for possible differences in the transverse relaxation of each phase and does not require the transfer of water from one phase to the other to realise a functional signal change. Secondly, the time-course of the SDP expansion-coefficient presented by Le Bihan *et al.* demonstrated a fast rise and return-to-baseline that always preceded the (GE) BOLD response by 1.5–3.5 s. This is in contrast to the timing characteristics of the SDP response observed in this paper, where no clear time-difference was apparent for the SDP time-course and raw $b=0$ (no diffusion-weighting) response. The onset of the SDP time-course occurred at about the same time as the rise in the $b=0$ response, and the return-to-baseline was relatively slow, taking ~20 s in comparison to the ~10 s of Le Bihan *et al.*'s SDP expansion coefficients. It should also be noted that, using hypercapnia and a sequence similar to that of Le Bihan *et al.*, recent experiments suggested that the high *b*-value functional signal change is largely due to the haemodynamic response rather than neuronal cell-swelling (30).

Tissue diffusion, non-exponential signal attenuation and BOLD fMRI

The origin of the non-exponential signal attenuation in brain tissue with respect to *b*-value remains obscure. Early studies posited the existence of two distinct water compartments, possibly corresponding to the extra- and intracellular spaces (10,12,15–18). Other researchers have remarked that there may be a more subtle separation of tissue water at a subcellular scale, where interactions between water molecules and intracellular structures lead to the formation of coexisting slow and fast diffusing phases (17,37,38). At the same time, a number of models have been proposed where non-monoexponential decay emerges without the need for a classification of tissue water into two pools (e.g. References (11,13,14,39–42)). In this case, the mechanism most commonly used to explain the non-exponential decay is motion restricted or hindered by tissue microstructure. As well as the free diffusion coefficient of the diffusing medium, these models are usually characterised by a number of parameters somehow related to the dimensions of the impeding boundaries.

The model presented in eqns (1)–(3) is built upon a simple system of two independent tissue-water pools, each with its own unique diffusion coefficient. As proposed in the previous section, the three time-dependent parameters of this model have a relatively straightforward interpretation in terms of the BOLD model, and diffusion-weighting can be used to decompose the separate contributions. On the other hand, even though it stands to reason that BOLD always contributes to SE DW-fMRI signal changes, the correspondence between BOLD and the model parameters is not immediately clear if a restricted-diffusion model is used to describe the diffusion-attenuated signal from brain tissue. As currently understood, EV BOLD signal changes are calculated for water motion around vessels in an isotropic, homogeneous medium characterised by a single diffusion constant. If it is found that a compartmental model does not sufficiently describe the signal attenuation, then some re-evaluation of the BOLD model may be necessary so that it is consistent with the properties of water diffusion in brain tissue.

Overall, it is not yet clear what determines the scales of molecular motion in a brain tissue; that is, whether the diffusion coefficients are determined by the physics of water at the cellular scale, such as in the model discussed by Le Bihan *et al.* (8,38), or whether water motion constrained by subcellular microstructure is more important. Restricted or hindered diffusion must have some influence on the NMR signal because there is a strong correlation between diffusion-tensor imaging and the organisation of white matter pathways. On the other hand, the different behaviours of the PSU and PSCR as a function of *b*-value indicate that there could be a distinct separation of tissue water motion into fast and slow regimes, making a multipool description of brain diffusion also possible. Whatever the case, a successful tissue model must not only describe the non-exponential tissue decay, but must also be consistent with the dependence of the functional signal changes observed when diffusion-weighting is applied. Understanding the roles of tissue structure and the cell-level physics of water in causing the non-exponential signal attenuation is important for applications of water diffusion as a tool for functional brain imaging.

CONCLUSIONS

The application of significant diffusion-weighting during the acquisition of fMRI data found that the PSCR and PSU follow different trends as a function of *b*-value, suggesting that they originate from disparate sources. The functional response has been interpreted in terms of a three compartment model. One compartment is purely vascular (FIV) while the other two (FDP and SDP) are dominated by brain tissue characterised by fast and slow diffusion constants. Repeating fMRI experiments at different *b*-values enables the decomposition of the stimulus-induced signal changes into FIV, FDP and SDP contributions. The FDP component demonstrated a substantial PSU, while the SDP signal change was highly reproducible and correlated with the stimulus uncontaminated by the undershoot. The FDP and SDP time-courses have been interpreted in terms of EV SE-BOLD signal changes. It was speculated that the SDP reflects EV SE-BOLD changes in small capillaries while the FDP corresponds to EV SE-BOLD changes in arteriole- or venule-sized vessels and/or an IV BOLD contribution from smaller veins where the blood velocity is slowest. A possible contribution to the SDP from the cell-swelling effect cannot yet be ruled out.

LIST OF SYMBOLS

b	diffusion-weighting in s/mm^2
D	arbitrary diffusion coefficient
D_f	diffusion coefficient for the fast-diffusion phase
D_s	diffusion coefficient for the slow-diffusion phase
R	vessel radius
S	total NMR signal originating from brain
S_{EV}	NMR signal originating from the extravascular compartment
S_{FDP}	NMR signal originating from the fast-diffusion phase
S_{FIV}	NMR signal originating from the fast intravascular compartment
S_{IV}	total NMR signal originating from the intravascular compartment
S_{SDP}	NMR signal originating from the slow-diffusion phase
t	time
T_2	transverse relaxation time
T_2^*	apparent transverse relaxation time
β	used in scaling law

Acknowledgements

The authors would like to thank R. Allen Waggoner for valuable discussion and criticism during the writing of this paper. Thanks are also extended to Yoko Kanazawa and Norihiko Fujita for insightful comments. This study was supported by a grant from the Ministry of Education, Culture, Sports, Science and Technology (MEXT), Japanese Government.

REFERENCES

1. Stejskal EO, Tanner JE. Spin diffusion measurements: spin echoes in the presence of a time-dependent field gradient. J. Chem. Phys. 1965; 42: 288–292.
2. Le Bihan D, Breton E, Lallemand D, Aubin M-L, Vignaud J, Laval-Jeantet M. Separation of diffusion and perfusion in intravoxel incoherent motion MR imaging. Radiology 1988; 168: 497–505.
3. Callaghan PT. *Principles of Nuclear Magnetic Resonance Spectroscopy*. Oxford University Press: New York, 1991; 362.
4. Gangstead SL, Song AW. On the timing characteristics of the apparent diffusion coefficient contrast in fMRI. Magn. Reson. Med. 2002; 48: 385–388.
5. Song AW, Woldorff MG, Gangstead S, Mangun GR, McCarthy G. Enhanced spatial localization of neuronal activation using simultaneous apparent-diffusion-coefficient and blood-oxygenation functional magnetic resonance imaging. Neuroimage 2002; 17: 742–750.
6. Harshbarger TB, Song AW. Endogenous functional CBV contrast revealed by diffusion weighting. NMR Biomed. 2006; 19: 1020–1027.
7. Darquie A, Poline JB, Poupon C, Saint-Jalmes H, Le Bihan D. Transient decrease in water diffusion observed in human occipital cortex during visual stimulation. Proc. Natl. Acad. Sci. U.S.A. 2001; 98: 9391–9395.
8. Le Bihan D, Urayama S, Aso T, Hanakawa T, Fukuyama H. Direct and fast detection of neuronal activation in the human brain with diffusion MRI. Proc. Natl. Acad. Sci. U.S.A. 2006; 103: 8263–8268.
9. Jin T, Zhao F, Kim S-G. Sources of functional apparent diffusion coefficient changes investigated by diffusion-weighted spin-echo fMRI. Magn. Reson. Med. 2006; 56: 1283–1292.
10. Chin CL, Wehrli FW, Fan Y, Hwang SN, Schwartz ED, Nissanov J, Hackney DB. Assessment of axonal fiber tract architecture in excised rat spinal cord by localized NMR q-space imaging: simulations and experimental studies. Magn. Reson. Med. 2004; 52: 733–740.
11. Kroenke CD, Ackerman JJ, Yablonskiy DA. On the nature of the NAA diffusion attenuated MR signal in the central nervous system. Magn. Reson. Med. 2004; 52: 1052–1059.
12. Niendorf T, Dijkhuizen RM, Norris DG, van Lookeren Campagne M, Nicolay K. Biexponential diffusion attenuation in various states of brain tissue: implications for diffusion-weighted imaging. Magn. Reson. Med. 1996; 36: 847–857.
13. Sukstanskii AL, Yablonskiy DA, Ackerman JJ. Effects of permeable boundaries on the diffusion-attenuated MR signal: insights from a one-dimensional model. J. Magn. Reson. 2004; 170: 56–66.
14. Yablonskiy DA, Bretthorst GL, Ackerman JJ. Statistical model for diffusion attenuated MR signal. Magn. Reson. Med. 2003; 50: 664–669.
15. Buckley DL, Bui JD, Phillips MI, Zelles T, Inglis BA, Plant HD, Blackband SJ. The effect of ouabain on water diffusion in the rat hippocampal slice measured by high resolution NMR imaging. Magn. Reson. Med. 1999; 41: 137–142.
16. Brugieres P, Thomas P, Maraval A, Hosseini H, Combes C, Chafiq A, Ruel L, Breil S, Peschanski M, Gaston A. Water diffusion compartmentation at high b values in ischemic human brain. AJNR Am. J. Neuroradiol. 2004; 25: 692–698.
17. Inglis BA, Bossart EL, Buckley DL, Wirth ED, III, Mareci TH. Visualisation of neural tissue water compartments using biexponential diffusion tensor MRI. Magn. Reson. Med. 2001; 45: 580–587.
18. Sehy JV, Ackerman JJH, Neil JJ. Evidence that both fast and slow water ADC components arise from intracellular space. Magn. Reson. Med. 2002; 48: 765–770.
19. Jochimsen TH, Norris DG, Mildner T, Möller HE. Quantifying the intra- and extravascular contributions to spin-echo fMRI at 3 T. Magn. Reson. Med. 2004; 52: 724–732.
20. Neil JJ, Ackerman JJH. Detection of pseudodiffusion in rat brain following blood substitution with perfluorocarbon. J. Magn. Reson. 1992; 97: 194–201.
21. Duong TQ, Kim S-G. In vivo MR measurements of regional arterial and venous blood volume fractions in intact rat brain. Magn. Reson. Med. 2000; 43: 393–402.
22. Kärger J, Pfeifer H, Heink W. Principles and application of self-diffusion measurements by nuclear magnetic resonance. Adv. Magn. Reson. 1988; 12: 1–89.
23. Mulkern RV, Gudbjartsson H, Westin C-f, Zengingonul HP, Gartner W, Guttmann CRG, Robertson RL, Kyriakos W, Scwartz R, Holtzman D, Jolesz FA, Maier SE. Multi-component apparent diffusion coefficients in human brain. NMR Biomed. 1999; 12: 51–62.
24. Mulkern RV, Zengingonul HP, Robertson RL, Bogner P, Zou KH, Gudbjartsson H, Guttmann CRG, Holtzman D, Kyriakos W, Jolesz FA, Maier SE. Multi-component apparent diffusion coefficient in human brain: relationship to spin-lattice relaxation. Magn. Reson. Med. 2000; 44: 292–300.
25. Clark CA, Le Bihan D. Water diffusion compartmentation and anisotropy at high b values in the human brain. Magn. Reson. Med. 2000; 44: 852–859.

26. Maier SE, Bogner P, Bajzik G, Mamata H, Mamata Y, Repa I, Jolesz FA, Mulkern RV. Normal brain and brain tumor: multicomponent apparent diffusion coefficient line scan imaging. Radiology 2001; 219: 842–849.
27. Mulkern RV, Vajapeyam S, Robertson RL, Caruso PA, Rivkin MJ, Maier SE. Biexponential apparent diffusion coefficient parametrization in adult vs newborn brain. Magn. Reson. Imaging 2001; 19: 659–668.
28. Le Bihan D, Breton E, Lallemand D, Grenier P, Cabanis E, Laval-Jeantet M. MR imaging of intravoxel incoherent motions: application to diffusion and perfusion in neurologic disorders. Radiology 1986; 161: 401–497.
29. Fujita N. Extravascular contribution of blood oxygenation level-dependent signal changes: a numerical analysis based on a vascular network model. Magn. Reson. Med. 2001; 46: 723–734.
30. Miller KL, Bulte DP, Devlin H, Robson MD, Wise RG, Woolrich MW, Jezzard P, Behrens TEJ. Evidence for a vascular contribution to diffusion fMRI at high *b*-value. Proc. Natl. Acad. Sci. U.S.A. 2007; 104: 20967–20972.
31. Yacoub E, Uludag K, Ugurbil K, Harel N. Decreases in ADC observed in tissue areas during activation in the cat visual cortex at 9.4 T using high diffusion sensitization. Magn. Reson. Imaging 2008; 26: 889–896.
32. Ogawa S, Menon RS, Tank DW, Kim S-G, Merkle H, Ellermann JM, Ugurbil K. Functional brain mapping by blood oxygenation level-dependent contrast magnetic resonance imaging. A comparison of signal characteristics with a biophysical model. Biophys. J. 1993; 64: 803–812.
33. Kennan RP, Zhong J, Gore JC. Intravascular susceptibility contrast mechanisms in tissues. Magn. Reson. Med. 1994; 31: 9–21.
34. Weisskoff RM, Zuo CS, Boxerman JL, Rosen BR. Microscopic susceptibility variation and transverse relaxation: theory and experiment. Magn. Reson. Med. 1994; 31: 601–610.
35. Boxerman JL, Hamberg LM, Rosen BR, Weisskoff RM. MR contrast due to intravascular magnetic susceptibility perturbations. Magn. Reson. Med. 1995; 34: 555–566.
36. Cassot F, Lauwers F, Fouard C, Prohaska S, Lauwers-Cances V. A novel three-dimensional computer-assisted method for a quantitative study of microvascular networks of the human cerebral cortex. Microcirculation 2006; 13: 1–18.
37. Schwarcz A, Bogner P, Meric P, Correze J-L, Berente Z, Pal J, Gallyas F, Doczi T, Gillet B, Beloeil J-C. The existence of biexponential signal decay in magnetic resonance diffusion-weighted imaging appears to be independent of compartmentalization. Magn. Reson. Med. 2004; 51: 278–285.
38. Le Bihan D. The 'wet mind': water and functional neuroimaging. Phys. Med. Biol. 2007; 52: R57–R90.
39. Frøhlich AF, Østergaard L, Kiselev VG. Effect of impermeable boundaries on diffusion-attenuated MR signal. J. Magn. Reson. 2006; 179: 223–233.
40. Bennet KM, Hyde JS, Schmainda KM. Water diffusion heterogeneity index in the human brain is insensitive to the orientation of applied magnetic field gradients. Magn. Reson. Med. 2006; 56: 235–239.
41. Kiselev VG, Il'yasov KA. Is the 'biexponential diffusion' biexponential? Magn. Reson. Med. 2007; 57: 464–469.
42. Zhou XJ, Abdullah O, Baleanu D, Magin RL. Analysis of high *b*-value diffusion images using fractional order calculus. In *Proceedings of the 16th ISMRM*, 2008; 36.

Available online at www.sciencedirect.com
ScienceDirect
Nuclear Medicine and Biology 36 (2009) 239–246
NUCLEAR MEDICINE — AND — BIOLOGY
www.elsevier.com/locate/nucmedbio

In vivo evaluation of P-glycoprotein and breast cancer resistance protein modulation in the brain using [^{11}C]gefitinib☆

Kazunori Kawamura*, Tomoteru Yamasaki, Joji Yui, Akiko Hatori, Fujiko Konno, Katsushi Kumata, Toshiaki Irie, Toshimitsu Fukumura, Kazutoshi Suzuki, Iwao Kanno, Ming-Rong Zhang

Department of Molecular Probes, Molecular Imaging Center, National Institute of Radiological Sciences, Chiba 263-8555, Japan

Received 26 November 2008; received in revised form 12 December 2008; accepted 16 December 2008

Abstract

Gefitinib (Iressa) is a selective inhibitor of epidermal growth factor receptor (EGFR) tyrosine kinase. Recent studies confirmed that gefitinib interacted with the breast cancer resistance protein (BCRP) at submicromolar concentrations, whereas other multidrug transporters, including P-glycoprotein (P-gp), showed much lower reactivity toward gefitinib. Recently, many tracers for positron emission tomography (PET) have been prepared to study P-gp function in vivo; however, PET tracers had not been evaluated for both P-gp and BCRP modulation in the brain. Therefore, we evaluated in vivo brain penetration-mediated P-gp and BCRP in mice using [^{11}C]gefitinib. Co-injection with gefitinib (over 50 mg/kg), a nonspecific P-gp modulator cyclosporin A (50 mg/kg), and the dual P-gp and BCRP modulator GF120918 (over 5 mg/kg) induced an increase in the brain uptake of [^{11}C]gefitinib in mice 30 min after injection. In the PET study of mice, the radioactivity level in the brain with co-injection of GF120918 (5 mg/kg) was three- to fourfold higher than that in control after initial uptake. The radioactivity level in the brain in P-gp and Bcrp knockout mice was approximately eightfold higher than that in wild-type mice 60 min after injection. In conclusion, [^{11}C]gefitinib is a promising PET tracer to evaluate the penetration of gefitinib into the brain by combined therapy with P-gp or BCRP modulators, and into brain tumors. Furthermore, PET study with GF120918 is a promising approach for evaluating brain penetration-mediated P-gp and BCRP.

Keywords: P-gp; BCRP; [^{11}C]Gefitinib; GF120918; Cyclosporin A; Brain penetration

1. Introduction

ATP-binding cassette (ABC) transporters are membrane-embedded proteins that limit intracellular concentration of substrates by pumping them out of the cell through an active energy-dependent mechanism [1,2]. ABC Transporters that confer multidrug resistance include P-glycoprotein (P-gp; gene symbol ABCB1), multidrug resistance protein 1 (MRP1; gene symbol ABCC1), multidrug resistance protein 2 (MRP2; gene symbol ABCC2) and breast cancer resistance protein (BCRP; gene symbol ABCG2) [1,2]. Among them, P-gp and MRP family have been extensively investigated. Recently, BCRP was isolated from atypical multidrug-resistant MCF-7 human breast cancer cells [3] and is a high-capacity efflux transporter with wide substrate specificity recognizing molecules of either negative or positive charge, molecules of organic anions and molecules of sulfate conjugates [4]. BCRP is expressed in a variety of tissues with highest levels in the placenta and lower levels present in the liver, kidney, small intestine, brain, and ducts and lobules of the breast, thereby showing extensive overlap with the tissue distribution of P-gp [5–8]. This tissue localization indicates that BCRP plays an important rule in absorption (small intestine), distribution (placenta and blood–brain barrier) and elimination (liver and small intestine) of drugs [9]. Several studies have demonstrated the high level of expression of BCRP in the brain [7,9], and confocal microscopic analysis demonstrated the high level of

☆ This study was partially supported by consignment expenses from the Molecular Imaging Program from the Ministry of Education, Culture, Sports, Science and Technology (MEXT) of the Japanese Government.
* Corresponding author. Tel.: +81 43 206 3192; fax: +81 43 206 3261.
E-mail address: kawamur@nirs.go.jp (K. Kawamura).

0969-8051/$ – see front matter © 2009 Elsevier Inc. All rights reserved.
doi:10.1016/j.nucmedbio.2008.12.006

expression of BCRP at the luminal surface of the microvessel endothelium of the human brain [7]. This localization closely resembles that of P-gp at the blood–brain barrier. Furthermore, the substrate specificity of BCRP shows considerable overlap with that of P-gp [10], suggesting that BCRP has a similar role to P-gp in the pharmacokinetics of substrate drugs [11].

Gefitinib (Iressa, AstraZeneca, London, UK; Fig. 1) is a selective inhibitor of epidermal growth factor receptor (EGFR) tyrosine kinase and blocks the signal transduction pathways implicated in the proliferation and survival of cancer cells [12,13]. Recent studies confirmed that gefitinib interacted with BCRP at submicromolar concentrations (half-maximal inhibition of ABCG2-dependent Hoechst 33342 dye extrusion at about 400 nM [14]), whereas other multidrug transporters, P-gp and MRP1, showed much lower reactivity toward gefitinib [14]. Furthermore, gefitinib inhibits the transporter function of BCRP and reverses BCRP-mediated drug resistance both in vitro and in vivo [15,16].

Several MDR-reversing agents are in various stages of clinical development. First-generation modulators such as verapamil and cyclosporine A required a high dose of drugs to reverse MDR and were associated with unacceptable toxicity. Third-generation MDR modulators including GF120918 (elacridar; Fig. 1), XR9576 (tariquidar) and LY335979 (zosuquidar) were developed specifically to interact only with the P-gp [17–19]. Limitations to the use of these modulators include multiple and redundant cellular mechanisms of resistance, alternations in pharmacokinetics of cytotoxic agents, and clinical toxicities. Among third-generation MDR modulators, GF120918, an acridone carboxamide derivative, is active at a concentration of around 20 nM, which is about 100-fold more potent than cyclosporine A [17], and is also a potent BCRP modulator with the concentration reversing 90% of BCRP-mediated drug resistance of 50 nM [20–22]. Recently, GF120918 has undergone Phase I studies as an MDR converter [23,24].

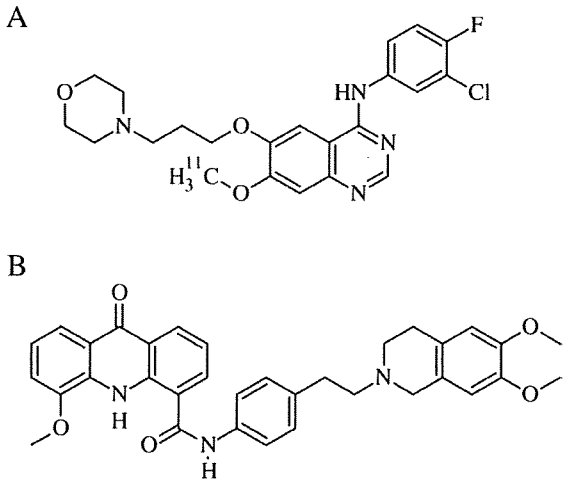

Fig. 1. Chemical structures of [^{11}C]gefitinib (A) and GF120918 (B).

Unlike several first-generation P-gp modulators (e.g., verapamil and cyclosporine A), GF120918 inhibits P-gp in vivo without significant toxicities or side effects [17].

Many tracers for positron emission tomography (PET) have been prepared to study P-gp function in vivo [25–27]. These include alkaloids ([^{11}C]colchicine) [28], antineoplastic agents ([^{11}C]daunorubicin [29], [^{18}F]paclitaxel [30]), modulators of L-type calcium channels ([^{11}C]verapamil [29,31]), β-adrenoceptor antagonists ([^{11}C](*S*)-carazolol [32], [^{18}F](*S*)-1′-fluorocarazolol [32], [^{11}C]carvedilol [33]), serotonin 5-HT_{1A} receptor antagonists ([^{18}F]MPPF [34], [^{11}C](*R*)-(−)-RWAY [35]), opioid receptor antagonists ([^{11}C]loperamide [36]), ^{64}Cu-labeled copper complexes [37,38] and ^{68}Ga-labeled complexes [39]. However, PET tracers had not been evaluated for both P-gp and BCRP modulation in the brain; therefore, we evaluated the in vivo brain penetration-mediated P-gp and BCRP in mice using [^{11}C]gefitinib.

2. Materials and methods

2.1. Materials

Gefitinib was prepared in our laboratory as previously described [40], as was GF120918 hydrochloride salt [41]. Cyclosporin A (Sandimmum) was purchased from Novartis Pharma (Basel, Switzerland). A solution of gefitinib was prepared in 10% hydroxypropyl-β-cyclodextrin solution and 5 mol/L HCl (adjusted to pH 5.0). A solution of GF120918 hydrochloride salt was prepared in distilled water. A solution of cyclosporine A was diluted with distilled water. All chemicals were from commercial sources.

[^{11}C]Gefitinib was synthesized by methylation of *O*-desmethyl gefitinib with [^{11}C]methyl triflate as previously described [42]. [^{11}C]Methyl iodide was prepared from [^{11}C] carbon dioxide via [^{11}C]methanol with an automated system as previously described [43]. [^{11}C]Methyl triflate was prepared by passing [^{11}C]methyl iodide through a glass column containing silver triflate at 180°C with a nitrogen gas flow. [^{11}C]Methyl triflate was trapped in the solution of acetone (0.3 ml) containing *O*-desmethyl gefitinib (0.3 mg) and 0.5 mol/L NaOH (2 μl) at room temperature. After evaporating acetone, 1.0 ml of the mixture of acetonitrile, water and triethylamine (25:25:0.1, v/v/v) was added, and the reaction mixture was applied to preparative high-performance liquid chromatography (HPLC), which was performed on a J'sphere ODS-H80 column (10 mm i.d.×250 mm length) (YMC, Kyoto, Japan) with UV detection at 254 nm, and with a mixture of acetonitrile, water and triethylamine (25:25:0.1, v/v/v) as the mobile phase at a flow rate of 5 ml/min. The retention time of [^{11}C]gefitinib was approximately 9 min. Specific activity was 40–85 TBq/mmol at the end of synthesis, and radiochemical purity was over 99%.

Male ddY mice (7–8 weeks old) were purchased from Japan SLC, Inc. (Shizuoka, Japan). Male P-gp and Bcrp

knockout (Mdr1a/1b(−/−) and Abcg(−/−)) mice [44] and male wild-type mice (FVB) were purchased from Taconic (Hudson, NY, USA). The animals were maintained and handled in accordance with recommendations by the US National Institutes of Health and our guidelines (National Institute of Radiological Sciences, Chiba, Japan). The animal studies were approved by the Animal Ethics Committee of National Institute of Radiological Sciences.

2.2. In vivo distribution studies in mice

[^{11}C]Gefitinib (3.8–8.2 MBq/68–150 pmol) was intravenously injected into ddY mice. The mice were sacrificed by cervical dislocation 30 min after injection. Blood was collected by heart puncture, and the tissues were dissected and weighed. The ^{11}C in samples was measured with an automatic gamma counter (Wizard 3″ 1480, PerkinElmer, Waltham, MA, USA). The tissue uptake of ^{11}C was expressed as the percent injected dose per gram of tissue (%ID/g).

The effects of the carrier dose or the dual P-gp and BCRP modulator GF120918 dose on the brain and blood were investigated. Mice (n=3–4) were co-injected with [^{11}C] gefitinib and different amounts of cold gefitinib (5, 50 and 100 mg/kg). As in another study, mice (n=3–4) were treated with intravenous injection of different amounts of GF120918 (5, 10, 30 and 50 mg/kg) 32–47 min prior to the [^{11}C] gefitinib intravenous injection.

The effects of pretreatment with P-gp and BCRP modulators on tissue distribution were investigated. Mice were treated with intravenous injection of one of the following P-gp and BCRP modulators, gefitinib (50 mg/kg), GF120918 (5 and 50 mg/kg) and cyclosporine A (50 mg/kg), 30–37 min prior to the injection. [^{11}C]Gefitinib was injected intravenously into control mice (n=7) and modulator-treated mice (n=3–5). The mice were sacrificed by cervical dislocation 30 min after injection.

The effects of the co-injection of P-gp and BCRP modulators on tissue distribution were investigated. [^{11}C] Gefitinib was intravenously injected into control mice (n=7) and co-injected with one of the following P-gp and BCRP modulators — gefitinib (50 mg/kg), GF120918 (5 mg/kg) and cyclosporine A (50 mg/kg) — into mice (n=3–4). The mice were sacrificed by cervical dislocation at 30 min after injection.

2.3. PET Study in mice

PET Measurement was performed in mice with an Inveon dedicated PET scanner (Siemens Healthcare, Erlangen, Germany). Mice were anesthetized with isoflurane (1.0%) and fixed in a prone position on the bed of the scanner. After a transmission scan to correct for attenuation, [^{11}C] gefitinib (16–36 MBq/0.30–0.61 nmol) was intravenously injected into mice, and a time-sequential scan was performed for 60 min (six frames per 10 s, four frames per 15 s, five frames per 1 min, four frames per 2 min, three frames per 5 min, three frames per 10 min).

Three normal ddY mice (7–8 weeks old, n=3) and three GF120918-treated ddY mice (7–8 weeks old, n=3) were used in this PET study. One normal mouse and GF120918-treated mouse were paired and scanned simultaneously on the scanner. In the GF120918 treatment study, [^{11}C]gefitinib was co-injected with GF120918 (5 mg/kg).

Three P-gp and Bcrp knockout mice (12–15 weeks old, 31–32 g, n=3) and three wild-type mice (12–15 weeks old, 28–35 g, n=3) were used in the PET study. One knockout mouse and one wild-type mouse were paired and scanned simultaneously on the scanner.

Decay-corrected radioactivity was expressed as the standardized uptake value [SUV, (tissue radioactivity/milliliter of tissue)/(injected radioactivity/gram of body weight)]. The area under the time–activity curve of the region of interests in the brain (AUC_{brain}, SUV·minute) was performed starting from 0 to 0.5 min, from 0.5 to 1 min, from 1 to 5 min, from 5 to 15 min, from 15 to 30 min and from 30 to 60 min, respectively.

2.4. Metabolite study in mice

[^{11}C]Gefitinib (40–57 MBq/1.1–1.6 nmol) was intravenously injected into ddY mice (n=3) and was intravenously co-injected with 5 mg/kg of GF120918 into ddY mice (n=3). They were sacrificed by cervical dislocation 30 min after injection. Blood was removed by heart puncture using a heparinized syringe and the brain was removed. The blood was centrifuged at 12,000 rpm (Model 5500, KUBOTA, Tokyo, Japan) for 3 min at 4°C to obtain plasma (0.2 ml), which was deproteinized with the same volume of an ice-cold acetonitrile. The mixture was then vortexed and centrifuged at 15,000 rpm for 2 min, and the supernatant was collected. The brain was homogenized in 0.5 ml of saline. After adding the same volume of acetonitrile to the homogenate, the mixture was vortexed and centrifuged at 15,000 rpm for 2 min, and the supernatant was collected. The supernatants were analyzed by HPLC with a radioactivity detector [45] on a Novapak C18 column (100×8 mm) (Waters, Milford, MA, USA) contained within a radial compression module (RCM-100, Waters) and eluted with mobile phase (acetonitrile/50 mM sodium acetate buffer, 40/60, v/v) at 2.0 ml/min. Radioactivity in the supernatants and in the residual precipitates after centrifugation and the radioactivity in the waste solution from HPLC were measured in an automatic gamma counter. The percentages of unchanged form were then determined.

2.5. Statistical analysis

Quantitative data are expressed as the mean±S.D. In the in vivo distribution study, differences between control groups and experimental groups were tested by one-way analysis of variance (ANOVA) and Dunnett's post hoc tests. In the PET study, different AUC_{brain} values between control mice and GF120918 loading mice or between wild-type mice and P-gp and Bcrp knockout mice were tested by

Student's t tests with Welch's correction. The analysis was performed with GraphPad Prism 5 software (GraphPad Software, La Jolla, CA, USA). Differences were considered significant when $P<05$.

3. Results

3.1. In vivo distribution studies in mice

To determine the effective dose of cold gefitinib and the dual P-gp and BCRP modulator GF120918, the dose effect of the pretreatment with gefitinib or co-injected with GF120918 on the brain-to-blood ratio of [^{11}C]gefitinib 30 min after injection was investigated in mouse brain and blood (Fig. 2). In the treatment with the lowest dose (5 mg/kg) of gefitinib, the brain-to-blood ratio was little affected; however, in the treatment with higher doses (50 and 100 mg/kg) of gefitinib, the brain-to-blood ratio increased three- and fourfold, respectively. Increasing doses of GF120198 caused a dose-dependent increase in the brain-to-blood ratio and showed no evidence of reaching a maximal effect at a 50 mg/kg dose of GF120918 intravenous pretreatment. In the treatment with the lowest dose (5 mg/kg) of GF120918, the brain-to-blood ratio increased fivefold. Furthermore, the brain-to-blood ratio in the treatment with the highest dose (50 mg/kg) of GF120918 increased about 12-fold.

Effects of pretreatment or co-injection with P-gp and BCRP modulators on the brain-to-blood ratio of radioactivity 30 min after injection of [^{11}C]gefitinib were investigated in mice (Fig. 3). In the pretreatment with a 5 mg/kg and a 50 mg/kg dose of GF120918, and a 50 mg/kg dose of cyclosporine A, the brain-to-blood ratio significantly increased; however, in the pretreatment with a 50 mg/kg dose of gefitinib, the brain-to-blood ratio was not affected. In co-injection with all investigated modulators, the brain-to-blood ratio significantly increased.

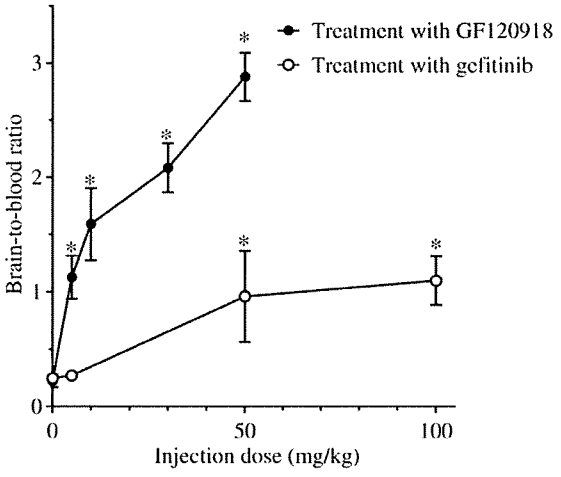

Fig. 2. Effects of treatment of gefitinib dose or GF120918 dose on the brain-to-blood ratio 30 min after injection of [^{11}C]gefitinib (3.8–8.2 MBq) into mice.

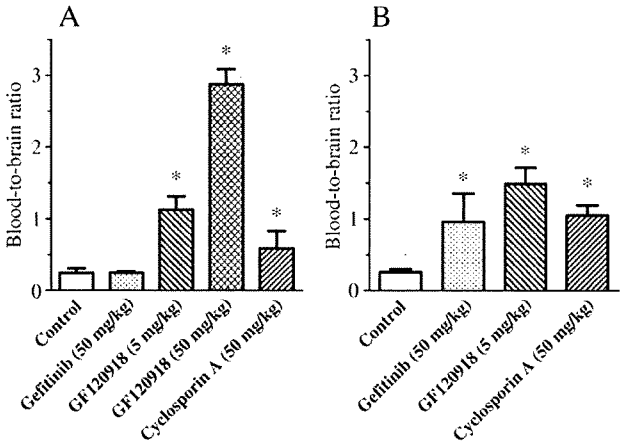

Fig. 3. Effects of pretreatment (A) or co-injection (B) with P-gp and BCRP modulators on the brain-to-blood ratio of radioactivity 30 min after injection of [^{11}C]gefitinib (3.8–8.2 MBq) into mice. Mean±S.D. (n=7 in control; n=3–4 in pretreatment studies; n=3–5 in co-injection studies). $P<05$ (one-way ANOVA and Dunnett's post hoc tests, compared with control).

Effects of pretreatment with P-gp and BCRP modulators on the tissue distribution of radioactivity 30 min after injection of [^{11}C]gefitinib into mice are summarized in Table 1. In the brain and muscle, pretreatment with all investigated modulators, except for gefitinib (50 mg/kg), induced a significant increase in uptake. In the blood and heart, pretreatment with a 50 mg/kg dose of cyclosporine A induced a significant increase in radioactivity. In the liver, pretreatment with a 50 mg/kg dose of GF120918 induced a significant increase in uptake. On the other hand, pretreatment with a 50 mg/kg dose of GF120918 induced a significant decrease of uptake in the lung. Also in the kidney, pretreatment with a 50 mg/kg dose of gefitinib induced a significant decrease in uptake.

Effects of co-injection with P-gp and BCRP modulators on the tissue distribution of radioactivity 30 min after injection of [^{11}C]gefitinib into mice are summarized in Table 2. In the brain, co-injection with all investigated modulators induced a significant increase in uptake. In the heart, co-injection with a 50 mg/kg dose of gefitinib induced a significant increase in uptake. In the liver, pretreatment with a 50 mg/kg dose of GF120918 induced a significant increase in uptake. In the muscle, pretreatment with a 5 mg/kg dose of GF120918 and 50 mg/kg dose of cyclosporine A induced a significant increase in uptake.

3.2. PET Studies in mice

Fig. 4 shows transaxial PET images of the brain using [^{11}C]gefitinib in mice. In control experiments (ddY and wild-type FVB mice), the radioactivity level in the brain was relatively low (Fig. 4A and C). By co-injection with GF120918 (5 mg/kg), the radioactivity level in the brain increased (Fig. 4B). In P-gp and Bcrp knockout mice, the radioactivity level in the brain increased (Fig. 4D).

Table 1
Effects of pretreatment with P-gp and BCRP modulators on the tissue distribution of radioactivity 30 min after injection of [^{11}C]gefitinib into mice

Tissue	Radioactivity level (%ID/g)[a]				
	Control	Gefitinib (50 mg/kg)	GF120918 (5 mg/kg)	GF120918 (50 mg/kg)	Cyclosporin A (50 mg/kg)
Brain	0.17±0.04	0.17±0.00	0.74±0.08*	1.80±0.13*	0.62±0.10*
Blood	0.69±0.13	0.68±0.05	0.67±0.11	0.63±0.03	1.16±0.40*
Heart	1.39±0.33	1.42±0.15	1.78±0.17	1.74±0.18	2.26±0.26*
Lung	15.90±2.06	14.70±5.79	18.27±1.39	7.85±1.74*	19.01±1.01
Liver	14.27±2.03	14.11±1.44	14.44±1.52	17.39±0.89*	14.94±0.83
Kidney	7.39±1.38	4.20±0.24*	7.41±1.25	5.47±0.58	7.57±1.09
Small intestine	12.32±4.67	7.34±2.69	8.93±3.10	7.30±0.66	13.26±3.38
Muscle	0.62±0.13	0.70±0.09	0.98±0.15*	0.90±0.07*	0.98±0.12*

[a] Mean±S.D. (n=7 in control; n=3–4 in pretreatment studies).
* P<05 (one-way ANOVA and Dunnett's post hoc tests, compared with control).

Fig. 5 shows the time–radioactivity curves of the brain in mice using [^{11}C]gefitinib. In control experiments (ddY and wild-type FVB mice), the radioactivity level in the brain decreased immediately after initial uptake and remained at constant level (Fig. 5A and B). In co-injection experiment with GF120918 (5 mg/kg), the radioactivity level in the brain was three- to fourfold higher than that in control experiment after initial uptake (Fig. 5A). After initial uptake, the radioactivity level in the brain in P-gp and Bcrp knockout mice increased gradually for 60 min after injection (Fig. 5B). The radioactivity level in the brain in P-gp and Bcrp knockout mice was approximately eightfold higher than that in wild-type mice 60 min after injection (Fig. 5B).

The area under the time–activity curve of the region of interests in the brain (AUC_{brain}) values in control mice, GF120918 loading (5 mg/kg) mice, wild-type mice and P-gp and Bcrp knockout mice is summarized in Table 3. The AUC_{brain} (0–0.5 min) value showed no significant difference between control mice and GF120918 loading mice, or between wild-type mice and P-gp and Bcrp knockout mice. The AUC_{brain} (0.5–1, 1–5, 5–15, 15–30 and 30–60 min) values in GF120918 loading mice and P-gp and Bcrp knockout mice were significantly higher than that in control mice or wild-type mice.

3.3. Metabolite study in mice

The metabolite study in brain tissue and plasma of mice 30 min after injection of [^{11}C]gefitinib was investigated. In the brain, the percentages of unchanged form were 88±1.9% (n=3) in control mice and 96±1.1% (n=3) in GF120918-treated mice, respectively. In the plasma, the percentages of unchanged form were 93±3.3% (n=3) in control mice and 89±4.8% (n=3) in GF120918-treated mice, respectively.

Table 2
Effects of co-injection with P-gp and BCRP modulators on the tissue distribution of radioactivity 30 min after injection of [^{11}C]gefitinib into mice

Tissue	Radioactivity level (%ID/g)[a]			
	Control	Gefitinib (50 mg/kg)	GF120918 (5 mg/kg)	Cyclosporin A (50 mg/kg)
Brain	0.18±0.03	0.79±0.20*	1.14±0.12*	0.79±0.19*
Blood	0.69±0.09	0.85±0.14	0.77±0.09	0.75±0.08
Heart	1.44±0.31	2.02±0.30*	1.76±0.26	1.93±0.48
Lung	14.89±2.83	12.27±1.18	16.38±2.57	17.47±3.35
Liver	13.64±1.89	15.18±1.21	16.04±2.10	13.31±1.79
Kidney	7.68±1.40	5.64±0.88	6.73±1.09	6.19±0.72
Small intestine	12.94±4.42	8.28±1.30	9.59±2.83	9.01±2.61
Muscle	0.61±0.14	0.73±0.38	0.96±0.09*	1.00±0.23*

[a] Mean±S.D. (n=7 in control; n=3–5 in co-injection studies).
* P<05 (one-way ANOVA and Dunnett's post hoc tests, compared with control).

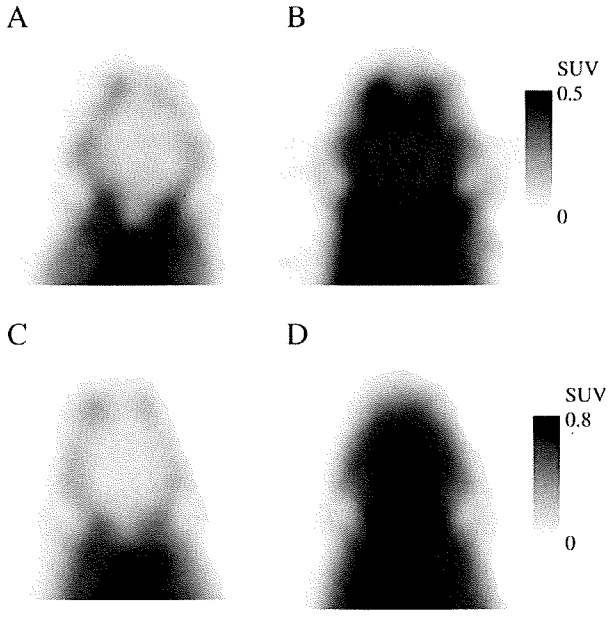

Fig. 4. Transaxial PET images of the brain using [^{11}C]gefitinib of control mouse (injected radioactivity, 24 MBq) (A), GF120918 (5 mg/kg) loading mouse (injected radioactivity, 24 MBq) (B), wild-type mouse (injected radioactivity, 32 MBq) (C), and P-gp and Bcrp knockout mouse (injected radioactivity, 31 MBq) (D). PET Images were acquired for 30 min, starting at 30 min after injection. Mice were anesthetized with isoflurane (1.0%) and were fixed in a prone position on the bed of the scanner.

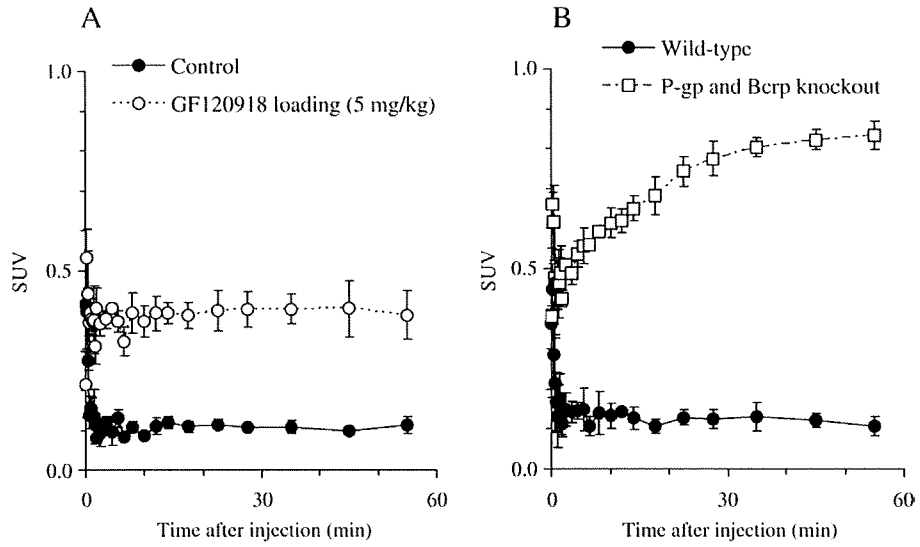

Fig. 5. Time–radioactivity curves of the brain in control mice and GF120918 (5 mg/kg) loading mice (A), and wild-type mice and P-gp and Bcrp knockout mice (B). Injected dose of [^{11}C]gefitinib was 16–36 MBq.

The recovery of radioactivity in HPLC analysis was essentially quantitative.

4. Discussion

In the present study, we evaluated P-gp and BCRP modulation in mice brain using [^{11}C]gefitinib. Co-injection or pretreatment with 50 mg/kg cyclosporine A, which is a nonspecific modulator of P-gp, induced an increase in the uptake of [^{11}C]gefitinib. Furthermore, co-injection or pretreatment with over 5 mg/kg of GF120918, which is a dual inhibitor of P-gp and BCRP, induced an increase in the uptake of [^{11}C]gefitinib. Co-injection with over 50 mg/kg of gefitinib induced an increase in the uptake of [^{11}C]gefitinib. Although gefitinib inhibited BCRP more potently than P-gp (10-fold) [14], it is considered that both transporters were modulated at an excess dose of gefitinib; therefore, these results suggest that the brain penetration of [^{11}C]gefitinib relates to both P-gp and BCRP.

Table 3
The area under the time–activity curve of the region of interests in the brain (AUC_{brain}) values in control mice, GF120918 loading (5 mg/kg) mice, wild-type mice, and P-gp and Bcrp knockout mice

Time after injection (min)	AUC_{brain} (SUV·min)[a]			
	Control	GF120918 loading (5 mg/kg)	Wild type	P-gp and Bcrp knockout
0–0.5	0.181±0.023	0.198±0.036	0.183±0.047	0.276±0.023
0.5–1	0.073±0.013	0.191±0.016*	0.086±0.039	0.233±0.023*
1–5	0.421±0.052	1.52±0.065*	0.583±0.127	2.00±0.076*
5–15	1.06±0.065	3.81±0.371*	1.34±0.307	6.07±0.270*
15–30	1.66±0.123	5.96±0.614*	1.81±0.307	11.0±0.579*
30–60	3.22±0.416	12.0±1.60*	3.61±0.755	24.6±0.709*

[a] Mean±S.D. (n=3).
* P<.05 (Student's t tests with Welch's correction, compared with control or wild-type mice).

In the PET study using [^{11}C]gefitinib, the time–radioactivity curves of the ddY mouse and wild-type FVB mouse brain showed fast washout from the brain after initial uptake. This result is explained by the rule of ABC transporters in limiting the brain penetration. Additionally, the AUC_{brain} (0–0.5 min) value showed no significant difference between control mice and GF120918 loading mice, or between wild-type mice and P-gp and Bcrp knockout mice, although AUC_{brain} (0.5–60 min) values in GF120918 loading mice and P-gp and Bcrp knockout mice were significantly higher than that in control mice or wild-type mice. This results also suggests that the PET study using [^{11}C]gefitinib demonstrates the rule of ABC transporter in limiting the brain penetration. By co-injection with 5 mg/kg GF120918, the radioactivity level in the brain was approximately three- to fourfold higher than that in control mice after initial uptake, and the AUC_{brain} value starting from 1 to 60 min was 3.7-fold higher than that in control mice. Furthermore, the radioactivity level in the brain in P-gp and Bcrp knockout mice was approximately eightfold higher than that in wild-type mice 60 min after injection, and the AUC_{brain} value starting from 15 to 60 min was 6.6-fold higher than that in wild-type mice; therefore, we demonstrated that brain penetration related to both P-gp and BCRP in the brain PET study. Many PET tracers have been prepared to study only P-gp function; however, some P-gp modulators, such as cyclosporine A and tariquidar, have a slight micromolar inhibitory concentration of BCRP [46]. Also, it was suggested that P-gp and BCRP work together to limit brain penetration [47]. It is considered that the function of

both P-gp and BCRP may be important in evaluating brain penetration in vivo.

In the present study, the effective dose of GF120918 for P-gp and BCRP modulation was lower than that of cyclosporine A. It was reported that GF120918 is a good alternative to cyclosporine A administration in enhancing the bioavailability of P-gp-mediated drugs [48]. Furthermore, GF120918 inhibits P-gp in vivo without significant toxicities or side effects [17]; therefore, it seems that a PET study combined with a clinically safe dose of GF120918 is a promising approach to improve brain penetration of PET probes for overcoming P-gp- and BCRP-mediated drug resistance.

Previously, the brain uptake of [^{11}C]verapamil, which is a PET tracer for P-gp function, in mice showed the largest increase by pretreatment with 50 mg/kg cyclosporine A 30 min before tracer injection [27]. In the present study, although pretreatment with 50 mg/kg cyclosporine A approximately 30 min before tracer injection induced a 3.6-fold increase in the brain uptake of [^{11}C]gefitinib, co-injection with 50 mg/kg cyclosporine A induced a 4.4-fold increase in the brain uptake of [^{11}C]gefitinib. Furthermore, co-injection with 5 mg/kg GF120918 induced a 6.3-fold increase in the brain uptake of [^{11}C]gefitinib, although pretreatment with 5 mg/kg GF120918 approximately 30 min before tracer injection induced a 4.4-fold increase in the brain uptake of [^{11}C]gefitinib. Additionally, co-injection with 50 mg/kg gefitinib induced a threefold increase in the brain uptake of [^{11}C]gefitinib, although the brain uptake of [^{11}C]gefitinib was not affected by pretreatment with 50 mg/kg gefitinib. This result may reveal that excess cold gefitinib inhibits the brain uptake of [^{11}C]gefitinib as an interaction between EGFR and ligand, and cause ligand-induced internalization of the EGFR [49–51]. It is considered that pretreatment with excess gefitinib induces a decrease in the brain uptake of [^{11}C]gefitinib binding EGFR by internalization and simultaneously induces an increase in the uptake of [^{11}C]gefitinib by the modulation of P-gp and BCRP. As a result, it seems that the total uptake of [^{11}C]gefitinib is little affected by pretreatment with excess gefitinib; therefore, it is considered that co-injection experiment with P-gp and BCRP modulators, such as GF120918, is a potent assay method for evaluating brain penetration-mediated P-gp and BCRP.

5. Conclusion

We demonstrated that the brain penetration of [^{11}C]gefitinib related to both P-gp and BCRP. From the results of the present study, [^{11}C]gefitinib is a promising PET tracer for evaluating the effect of brain penetration of gefitinib by combined therapy with P-gp or BCRP modulators and for evaluating the penetration of gefitinib into brain tumors. Furthermore, PET study with GF120918 is a promising approach for evaluating the brain penetration-mediated P-gp and BCRP.

Acknowledgments

We thank the staff of the Cyclotron Operation Section and Department of Molecular Probes, National Institute of Radiological Sciences (NIRS) for their technical assistance in radioisotope production. We also thank Mrs. Makoto Takei (Tokyo Nuclear Service), Ikuo Nakamura (Tokyo Nuclear Service) and Hisashi Suzuki (NIRS) for their technical assistance with the radiosynthesis of radiopharmaceuticals. We are grateful to Mr. Kazuhiko Yanamoto for his technical assistance with the in vivo distribution study and mouse PET study, and also to Mr. Hidekatsu Wakisaka for his technical assistance with the operation of the PET scanner.

References

[1] Gottesman MM, Fojo T, Bates SE. Multidrug resistance in cancer: role of ATP-dependent transporters. Nat Rev Cancer 2002;2:48–58.
[2] Borst P, Oude Elferink R. Mammalian ABC transporters in health and disease. Annu Rev Biochem 2002;71:537–92.
[3] Doyle LA, Yang W, Abruzzo LV, et al. A multidrug resistance transporter from human MCF-7 breast cancer cells. Proc Natl Acad Sci U S A 1998;95:15665–70.
[4] Staud F, Pavek P. Breast cancer resistance protein (BCRP/ABCG2). Int J Biochem Cell Biol 2005;37:720–5.
[5] Maliepaard M, Scheffer GL, Faneyte IF, van Gastelen MA, Pijnenborg AC, Schinkel AH, et al. Subcellular localization and distribution of the breast cancer resistance protein transporter in normal human tissues. Cancer Res 2001;61:3458–64.
[6] Jonker JW, Buitelaar M, Wagenaar E, Van Der Valk MA, Scheffer GL, Scheper RJ, et al. The breast cancer resistance protein protects against a major chlorophyll-derived dietary phototoxin and protoporphyria. Proc Natl Acad Sci U S A 2002;99:15649–54.
[7] Cooray HC, Blackmore CG, Maskell L, Barrand MA. Localisation of breast cancer resistance protein in microvessel endothelium of human brain. Neuroreport 2002;13:2059–63.
[8] Doyle LA, Ross DD. Multidrug resistance mediated by the breast cancer resistance protein BCRP (ABCG2). Oncogene 2003;22:7340–58.
[9] Mao Q, Unadkat JD. Role of the breast cancer resistance protein (ABCG2) in drug transport. AAPS J 2005;7:E118–33.
[10] Haimeur A, Conseil G, Deeley RG, Cole SP. The MRP-related and BCRP/ABCG2 multidrug resistance proteins: biology, substrate specificity and regulation. Curr Drug Metab 2004;5:21–53.
[11] Breedveld P, Beijnen JH, Schellens JH. Use of P-glycoprotein and BCRP inhibitors to improve oral bioavailability and CNS penetration of anticancer drugs. Trends Pharmacol Sci 2006;27:17–24.
[12] Baselga J, Averbuch SD. ZD1839 ('Iressa') as an anticancer agent. Drugs 2000;60:33–40.
[13] Arteaga CL, Johnson DH. Tyrosine kinase inhibitors—ZD1839 (Iressa). Curr Opin Oncol 2001;13:491–8.
[14] Özvegy-Laczka C, Hegedűs T, Várady G, Ujhelly O, Schuetz JD, Váradi A, et al. High-affinity interaction of tyrosine kinase inhibitors with the ABCG2 multidrug transporter. Mol Pharmacol 2004;65:1485–95.
[15] Yanase K, Tsukahara S, Asada S, Ishikawa E, Imai Y, Sugimoto Y. Gefitinib reverses breast cancer resistance protein-mediated drug resistance. Mol Cancer Ther 2004;3:1119–25.
[16] Nakamura Y, Oka M, Soda H, Shiozawa K, Yoshikawa M, Itoh A, et al. Gefitinib ("Iressa", ZD1839), an epidermal growth factor receptor tyrosine kinase inhibitor, reverses breast cancer resistance protein/ABCG2-mediated drug resistance. Cancer Res 2005;65:1541–6.

[17] Hyafil F, Vergely C, Du Vignaud P, Grand-Perret T. In vitro and in vivo reversal of multidrug resistance by GF120918, an acridonecarboxamide derivative. Cancer Res 1993;53:4595–602.
[18] Dantzig AH, Shepard RL, Cao J, Law KL, Ehlhardt WJ, Baughman TM, et al. Reversal of P-glycoprotein-mediated multidrug resistance by a potent cyclopropyldibenzosuberane modulator, LY335979. Cancer Res 1996;56:4171–9.
[19] Dale IL, Tuffley W, Callaghan R, Holmes JA, Martin K, Luscombe M, et al. Reversal of P-glycoprotein-mediated multidrug resistance by XR9051, a novel diketopiperazine derivative. Br J Cancer 1998;78:885–92.
[20] de Bruin M, Miyake K, Litman T, Robey R, Bates SE. Reversal of resistance by GF120918 in cell lines expressing the ABC half-transporter, MXR. Cancer Lett 1999;146:117–26.
[21] Jonker JW, Smit JW, Brinkhuis RF, Maliepaard M, Beijnen JH, Schellens JH, et al. Role of breast cancer resistance protein in the bioavailability and fetal penetration of topotecan. J Natl Cancer Inst 2000;92:1651–6.
[22] Allen JD, van Loevezijn A, Lakhai JM, van der Valk M, van Tellingen O, Reid G, et al. Potent and specific inhibition of the breast cancer resistance protein multidrug transporter in vitro and in mouse intestine by a novel analogue of fumitremorgin C. Mol Cancer Ther 2002;1:417–25.
[23] Planting AS, Sonneveld P, van der Gaast A, Sparreboom A, van der Burg ME, Luyten GP, et al. A phase I and pharmacologic study of the MDR converter GF120918 in combination with doxorubicin in patients with advanced solid tumors. Cancer Chemother Pharmacol 2005;55:91–9.
[24] Kuppens IE, Witteveen EO, Jewell RC, Radema SA, Paul EM, Mangum SG, et al. A phase I, randomized, open-label, parallel-cohort, dose-finding study of elacridar (GF120918) and oral topotecan in cancer patients. Clin Cancer Res 2007;13:3276–85.
[25] Elsinga PH, Hendrikse NH, Bart J, Vaalburg W, van Waarde A. PET Studies on P-glycoprotein function in the blood–brain barrier: how it affects uptake and binding of drugs within the CNS. Curr Pharm Des 2004;10:1493–503.
[26] Elsinga PH, Hendrikse NH, Bart J, van Waarde A, Vaalburg W. Positron emission tomography studies on binding of central nervous system drugs and P-glycoprotein function in the rodent brain. Mol Imaging Biol 2005;7:37–44.
[27] Ishiwata K, Kawamura K, Yanai K, Hendrikse NH. In vivo evaluation of P-glycoprotein modulation of 8 PET radioligands used clinically. J Nucl Med 2007;48:81–7.
[28] Levchenko A, Mehta BM, Lee JB, Humm JL, Augensen F, Squire O, et al. Evaluation of ^{11}C-colchicine for PET imaging of multiple drug resistance. J Nucl Med 2000;41:493–501.
[29] Elsinga PH, Franssen EJ, Hendrikse NH, Fluks L, Weemaes AM, van der Graaf WT, et al. Carbon-11-labeled daunorubicin and verapamil for probing P-glycoprotein in tumors with PET. J Nucl Med 1996;37:1571–5.
[30] Kurdziel KA, Kiesewetter DO, Carson RE, Eckelman WC, Herscovitch P. Biodistribution, radiation dose estimates, and in vivo Pgp modulation studies of ^{18}F-paclitaxel in nonhuman primates. J Nucl Med 2003;44:1330–9.
[31] Luurtsema G, Molthoff CF, Windhorst AD, Smit JW, Keizer H, Boellaard R, et al. (*R*)- and (*S*)-[^{11}C]verapamil as PET-tracers for measuring P-glycoprotein function: in vitro and in vivo evaluation. Nucl Med Biol 2003;30:747–51.
[32] Doze P, Van Waarde A, Elsinga PH, Hendrikse NH, Vaalburg W. Enhanced cerebral uptake of receptor ligands by modulation of P-glycoprotein function in the blood–brain barrier. Synapse 2000;36:66–74.
[33] Bart J, Dijkers EC, Wegman TD, de Vries EG, van der Graaf WT, Groen HJ, et al. New positron emission tomography tracer [^{11}C] carvedilol reveals P-glycoprotein modulation kinetics. Br J Pharmacol 2005;145:1045–51.
[34] Passchier J, van Waarde A, Doze P, Elsinga PH, Vaalburg W. Influence of P-glycoprotein on brain uptake of [^{18}F]MPPF in rats. Eur J Pharmacol 2000;407:273–80.
[35] Liow JS, Lu S, McCarron JA, Hong J, Musachio JL, Pike VW, et al. Effect of a P-glycoprotein inhibitor, Cyclosporin A, on the disposition in rodent brain and blood of the 5-HT1A receptor radioligand, [^{11}C](*R*)-(−)-RWAY. Synapse 2007;61:96–105.
[36] Zoghbi SS, Liow JS, Yasuno F, Hong J, Tuan E, Lazarova N, et al. ^{11}C-Loperamide and its *N*-desmethyl radiometabolite are avid substrates for brain permeability-glycoprotein efflux. J Nucl Med 2008;49:649–56.
[37] Lewis JS, Dearling JL, Sosabowski JK, Zweit J, Carnochan P, Kelland LR, et al. Copper bis(diphosphine) complexes: radiopharmaceuticals for the detection of multi-drug resistance in tumours by PET. Eur J Nucl Med 2000;27:638–46.
[38] Packard AB, Kronauge JF, Barbarics E, Kiani S, Treves ST. Synthesis and biodistribution of a lipophilic ^{64}Cu-labeled monocationic copper (II) complex. Nucl Med Biol 2002;29:289–94.
[39] Sharma V, Prior JL, Belinsky MG, Kruh GD, Piwnica-Worms D. Characterization of a ^{67}Ga/^{68}Ga radiopharmaceutical for SPECT and PET of MDR1 P-glycoprotein transport activity in vivo: validation in multidrug-resistant tumors and at the blood–brain barrier. J Nucl Med 2005;46:354–64.
[40] Gilday JP, Moody D. Process for the preparation of 4-(3′-chlorp-4′-fluoroanilino)-7-methoxy-6-(3-morpholinopropoxy) quinazoline. PCT Int Appl 2004:A1 WO/2004/024703.
[41] Dodic N, Dumaitre B, Daugan A, Pianetti P. Synthesis and activity against multidrug resistance in Chinese hamster ovary cells of new acridone-4-carboxamides. J Med Chem 1995;38:2418–26.
[42] Wang JQ, Gao M, Miller KD, Sledge GW, Zheng QH. Synthesis of [^{11}C]Iressa as a new potential PET cancer imaging agent for epidermal growth factor receptor tyrosine kinase. Bioorg Med Chem Lett 2006;16(15):4102–6.
[43] Suzuki K, Inoue O, Hashimoto K, Yamasaki T, Kuchiki M, Tamate K. Computer-controlled large scale production of high specific activity [^{11}C]Ro15-1788. Appl Radiat Isot 1985;36:971–6.
[44] Jonker JW, Freeman J, Bolscher E, Musters S, Alvi A, Titley I, et al. Contribution of the ABC transporters Bcrp1 and Mdr1a/1b to the side population phenotype in mammary gland and bone marrow of mice. Stem Cells 2005;23:1059–65.
[45] Takei M, Kida T, Suzuki K. Sensitive measurement of positron emitters eluted from HPLC. Appl Radiat Isot 2001;55:229–34.
[46] Pick A, Müller H, Wiese M. Structure–activity relationships of new inhibitors of breast cancer resistance protein (ABCG2). Bioorg Med Chem 2008;16:8224–36.
[47] de Vries NA, Zhao J, Kroon E, Buckle T, Beijnen JH, van Tellingen O. P-Glycoprotein and breast cancer resistance protein: two dominant transporters working together in limiting the brain penetration of topotecan. Clin Cancer Res 2007;13:6440–9.
[48] Malingré MM, Beijnen JH, Rosing H, Koopman FJ, Jewell RC, Paul EM, et al. Co-administration of GF120918 significantly increases the systemic exposure to oral paclitaxel in cancer patients. Br J Cancer 2001;84:42–7.
[49] Carpenter G, Cohen S. ^{125}I-Labeled human epidermal growth factor. Binding, internalization, and degradation in human fibroblasts. J Cell Biol 1976;71:159–71.
[50] Haigler HT, McKanna JA, Cohen S. Direct visualization of the binding and internalization of a ferritin conjugate of epidermal growth factor in human carcinoma cells A-431. J Cell Biol 1979;81:382–95.
[51] Wiley HS. Trafficking of the ErbB receptors and its influence on signaling. Exp Cell Res 2003;284:78–88.

J Neurosurg 111:28–36, 2009

Analysis of cerebral perfusion and metabolism assessed with positron emission tomography before and after carotid artery stenting

Clinical article

Shunji Matsubara, M.D., Ph.D.,[1] Junta Moroi, M.D., Ph.D.,[1] Akifumi Suzuki, M.D., Ph.D.,[1] Masahiro Sasaki, M.D., Ph.D.,[1] Ken Nagata, M.D., Ph.D.,[1] Iwao Kanno, Ph.D.,[2] and Shuichi Miura, Ph.D.[2]

Departments of [1]Strokology, and [2]Radiology and Nuclear Medicine, Research Institute for Brain and Blood Vessels–Akita, Akita, Japan

Object. The authors analyzed cerebral perfusion and metabolism in patients with internal carotid artery stenosis before and after carotid artery stenting (CAS).

Methods. Sixteen patients with internal carotid artery stenosis (> 70%) underwent PET scanning before CAS, 1–7 days after CAS, and 3–4 months after CAS to assess a variety of parameters related to cerebral perfusion and metabolism.

Results. Cerebral blood flow at rest (CBF_{rest}) significantly increased in the immediate postoperative stage before returning to normal levels over the long term; this trend was also recognized on the contralateral side. In contrast, there was gradual improvement in the rate of CBF variation on acetazolamide administration (% CBF_{az}). Cerebral perfusion pressure (CBF/cerebral blood volume) increased rapidly during the acute stage and decreased in the long term, and the oxygen extraction fraction decreased slightly during the acute stage before normalizing over the long term. The cerebral metabolic rate of oxygen ($CMRO_2$) increased slightly after stenting over both the short and long term. The ratios of ipsilateral to contralateral values (asymmetry index) for CBF_{rest}, % CBF_{az}, cerebral blood volume, oxygen extraction fraction, and $CMRO_2$ tended to approach 1.0 over time.

Conclusions. Repeated PET scanning revealed improvements in CBF, perfusion pressure, and oxygen metabolism after CAS. In particular, the vascular reserve tended to improve gradually, while CBF, cerebral perfusion pressure, and $CMRO_2$ increased rapidly and peaked soon after CAS. These results suggest that a large discrepancy between rapidly increased CBF, perfusion pressure, and a small increase in vascular reserve in the acute stage after CAS could cause hyperperfusion syndrome. *(DOI: 10.3171/2008.09.17663)*

Key Words • **carotid artery stenting** • **cerebral blood flow** • **hyperperfusion** • **PET** • **vascular reserve**

Internal CA stenosis sometimes causes cerebral ischemia either due to hemodynamic hypoperfusion or an artery-to-artery embolism. Although antiplatelet and/or anticoagulant pharmacotherapies are standard initial treatments for this disorder, CEA has been declared the gold standard not only for symptomatic ICA stenosis (≤ 70%),[26] but also for asymptomatic ICA stenosis (≤ 60%).[4]

Abbreviations used in this paper: CA = carotid artery; CAS = CA stenting; CBF = cerebral blood flow; CBF_{az} = CBF after acetazolamide challenge; CBF_{rest} = CBF at rest; CBV = cerebral blood volume; CEA = carotid endarterectomy; $CMRO_2$ = cerebral metabolic rate of oxygen; CPP = cerebral perfusion pressure; ICA = internal carotid artery; OEF = oxygen extraction fraction.

Carotid artery stenting was used in only a limited number of patients until several years ago because of the risk of intraoperative embolic cerebral ischemia. The recent development of protective devices has markedly improved treatment results,[9] and the current low rate of complications associated with CAS is mainly due to total protection systems such as PercuSurge GuardWire devices.[13,28] In addition, data from the Stenting and Angioplasty with Protection in Patients at High Risk for Endarterectomy Study[24] have demonstrated that CAS with an embolus protection device is not inferior to CEA in patients with severe CA stenosis and comorbidities. However, investigators in another recent multicenter trial of the use of

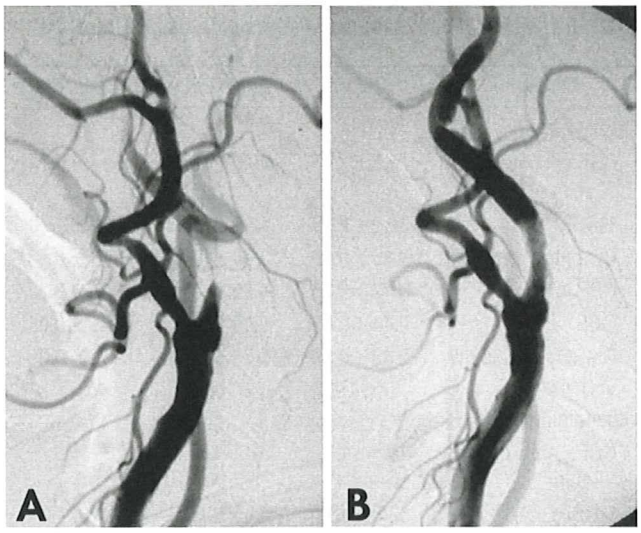

FIG. 1. Images obtained in the 71-year-old woman in the representative case. Preoperative right carotid injection angiogram confirming severe ICA stenosis (A). Right CA stenting was performed via the femoral artery without neurological sequelae. Postoperative angiography demonstrated no significant residual stenosis (B).

CAS with or without a protection device failed to prove safety compared to CEA.[36]

With respect to cerebral perfusion, analysis of SPECT data before and after CEA has revealed improvements in postoperative vasoreactivity,[2,15,16,34] but little is known about alterations in cerebral perfusion before and after CAS.[5,17,20] No previous studies have examined cerebral perfusion and metabolism on PET, with the exception of a small number of case reports describing distal ICA and basilar artery stenosis.[3,19,33] The present study is the first to describe alterations in cerebral perfusion and metabolism on PET scans obtained before and after CAS in patients with ICA stenosis.

Methods

Patient Population

Thirty-one patients with ICA stenosis ≥ 70% underwent CAS at our institution for a total of 34 lesions between April 2002 and March 2004. Positron emission tomography scanning was conducted before and after CAS in 28 lesions. Patients with coexisting conditions such as contralateral severe ICA stenosis or occlusion, or ipsilateral middle cerebral artery or distal ICA stenosis were excluded. Sixteen patients with 16 lesions participated in this study, including 12 men and 4 women with a mean age of 71.1 years (range 55–78 years) harboring 5 symptomatic and 11 asymptomatic lesions.

Protocol for CAS

A PercuSurge GuardWire system (Medtronic) was

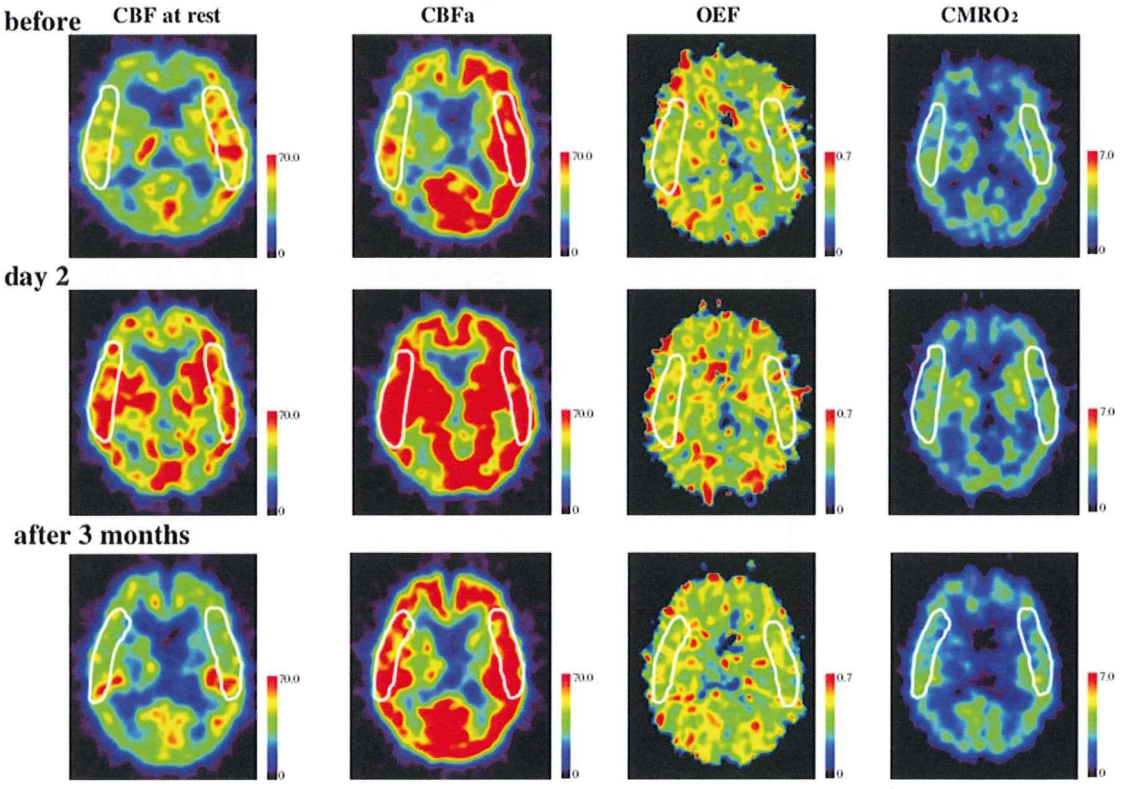

FIG. 2. Series of PET studies. *Upper Row:* Preoperative examinations detecting hypoperfusion and low vascular reserve in CBF_{rest} and CBF_{az}. No significant lateralities were noted in cerebral oxygen metabolism (OEF and $CMRO_2$). *Middle Row:* Studies obtained on postoperative Day 2 demonstrating a marked increase in CBF_{rest} and CBF_{az}, particularly on the affected side. The $CMRO_2$ increased subtly on the affected side. *Bottom Row:* Postoperative examination obtained 3 months after CAS confirming the absence of laterality for CBF_{rest} and improvements in CBF_{az}.